Article

Molecular Cell

A Non-amyloid Prion Particle that Activates a Heritable Gene Expression Program

Graphical Abstract

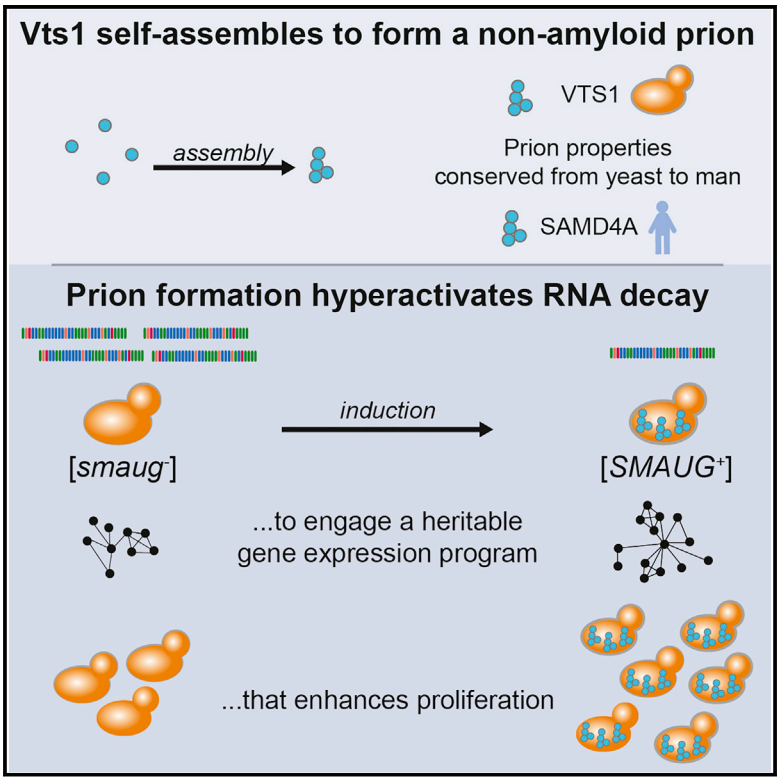

Highlights

- The Vts1 IDR promotes its condensation into the non-amyloid prion [*SMAUG*$^{+}$]
- [*SMAUG*$^{+}$] hyperactivates Vts1 function
- [*SMAUG*$^{+}$] rewires post-transcriptional gene regulation to promote proliferation
- Self-assembly is conserved in the human Vts1 homolog hSmaug1

Authors

Anupam K. Chakravarty, Tina Smejkal, Alan K. Itakura, David M. Garcia, Daniel F. Jarosz

Correspondence

jarosz@stanford.edu

In Brief

Chakravarty et al. define a new mechanism in protein-based epigenetics. Self-assembly of the evolutionarily ancient RNA-binding protein Vts1/Smaug drives formation of a non-amyloid prion, [*SMAUG*$^{+}$], that heritably activates protein function. [*SMAUG*$^{+}$] rewires post-transcriptional gene expression landscapes to favor robust mitotic growth. Its self-assembly properties are conserved across eukaryotes.

Chakravarty et al., 2020, Molecular Cell 77, 1–15
January 16, 2020
https://doi.org/10.1016/j.molcel.2019.10.028

CellPress

Please cite this article in press as: Chakravarty et al., A Non-amyloid Prion Particle that Activates a Heritable Gene Expression Program, Molecular Cell (2019), https://doi.org/10.1016/j.molcel.2019.10.028

Molecular Cell
Article

A Non-amyloid Prion Particle that Activates a Heritable Gene Expression Program

Anupam K. Chakravarty,[1] Tina Smejkal,[1,4] Alan K. Itakura,[2] David M. Garcia,[1,5] and Daniel F. Jarosz[1,3,6,*]
[1]Department of Chemical and Systems Biology, Stanford University, 269 Campus Drive, Stanford, CA 94305, USA
[2]Department of Biology, Stanford University, 269 Campus Drive, Stanford, CA 94305, USA
[3]Department of Developmental Biology, Stanford University, 269 Campus Drive, Stanford, CA 94305, USA
[4]Present address: Bayreuther Strasse 9, 01187 Dresden, Germany
[5]Present address: Institute of Molecular Biology, University of Oregon, 1318 Franklin Boulevard, Eugene, OR 97403, USA
[6]Lead Contact
*Correspondence: jarosz@stanford.edu
https://doi.org/10.1016/j.molcel.2019.10.028

SUMMARY

Spatiotemporal gene regulation is often driven by RNA-binding proteins that harbor long intrinsically disordered regions in addition to folded RNA-binding domains. We report that the disordered region of the evolutionarily ancient developmental regulator Vts1/Smaug drives self-assembly into gel-like condensates. These proteinaceous particles are not composed of amyloid, yet they are infectious, allowing them to act as a protein-based epigenetic element: a prion [*SMAUG*$^{+}$]. In contrast to many amyloid prions, condensation of Vts1 enhances its function in mRNA decay, and its self-assembly properties are conserved over large evolutionary distances. Yeast cells harboring [*SMAUG*$^{+}$] downregulate a coherent network of mRNAs and exhibit improved growth under nutrient limitation. Vts1 condensates formed from purified protein can transform naive cells to acquire [*SMAUG*$^{+}$]. Our data establish that non-amyloid self-assembly of RNA-binding proteins can drive a form of epigenetics beyond the chromosome, instilling adaptive gene expression programs that are heritable over long biological timescales.

INTRODUCTION

All organisms must coordinate gene regulation in time and space across a crowded intracellular milieu. Many components of this circuitry are RNA-binding proteins (RBPs; Gerstberger et al., 2014; Nishtala et al., 2016), post-transcriptional regulators that dictate the fate of every mRNA (Bartel, 2009; Campbell and Wickens, 2015; Castello et al., 2012; Glisovic et al., 2008; Ray et al., 2013). Many RBPs have a conspicuous architecture: an ordered RNA interaction domain coupled to a large intrinsically disordered region (IDR; Calabretta and Richard, 2015). By contrast to the ordered RNA-binding domains, the impact of IDRs within RBPs remains mostly enigmatic (Draper, 1999; Hentze et al., 2018; Stefl et al., 2005).

Intrinsically disordered proteins—those with large IDRs—are common in eukaryotes (Uversky, 2014; van der Lee et al., 2014). Some IDPs can coalescence into biomolecular condensates (Banani et al., 2017; Hyman et al., 2014; Molliex et al., 2015; Protter et al., 2018), a "phase separation" behavior hypothesized to locally arrange the cytoplasm and the nucleoplasm (Brangwynne, 2013; Uversky, 2017; Zhu and Brangwynne, 2015). Such condensates, which often form in response to environmental stimuli (Franzmann et al., 2018; Riback et al., 2017), can also act as hubs of cellular signaling (Banjade and Rosen, 2014; Li et al., 2012) and are emerging as an organizing principle in cell biology (Alberti, 2017; Shin and Brangwynne, 2017; Smith et al., 2016).

Many IDRs have low sequence complexity and are prone to forming high-order assemblies (Molliex et al., 2015). These sequences are often termed prion-like based on enrichment for asparagine and glutamine residues (Alberti et al., 2009). Yet, condensates formed by most prion-like RBPs are not heritable (March et al., 2016). By contrast, bona fide prions can switch between multiple conformations, at least one of which self-templates (Glover et al., 1997; Prusiner, 1984), and thus persist over long biological timescales.

Although prions provide a paradigm-shifting mechanism of information transfer, they were long considered to be rare. However, their recent discovery throughout life suggests that this form of inheritance may be common and evolutionarily ancient (Chakravarty and Jarosz, 2018; Halfmann et al., 2010; Liebman and Chernoff, 2012). In the budding yeast *Saccharomyces cerevisiae*, prions operate as epigenetic elements that can couple the emergence of new phenotypes to environmental change (Harvey et al., 2018; Li and Kowal, 2012). The first prions discovered form amyloids, sequestering the native protein into fibrils (Alberti et al., 2009; Chernoff et al., 1995; Holmes et al., 2013; Suzuki et al., 2012; Toyama et al., 2007), and often inactivating the protein's function. Prions are inherited by mitotic and meiotic progeny alike (Aigle and Lacroute, 1975; Byers and Jarosz, 2014; Chakravarty and Jarosz, 2018; Cox, 1965; Griswold and Masel, 2009; Harvey et al., 2018; Jarosz and Khurana, 2017), allowing selection to enrich the ensuing phenotypes in future generations if they are adaptive.

Recently, we discovered a suite of intrinsically disordered RBPs in *S. cerevisiae* that can drive the emergence of traits

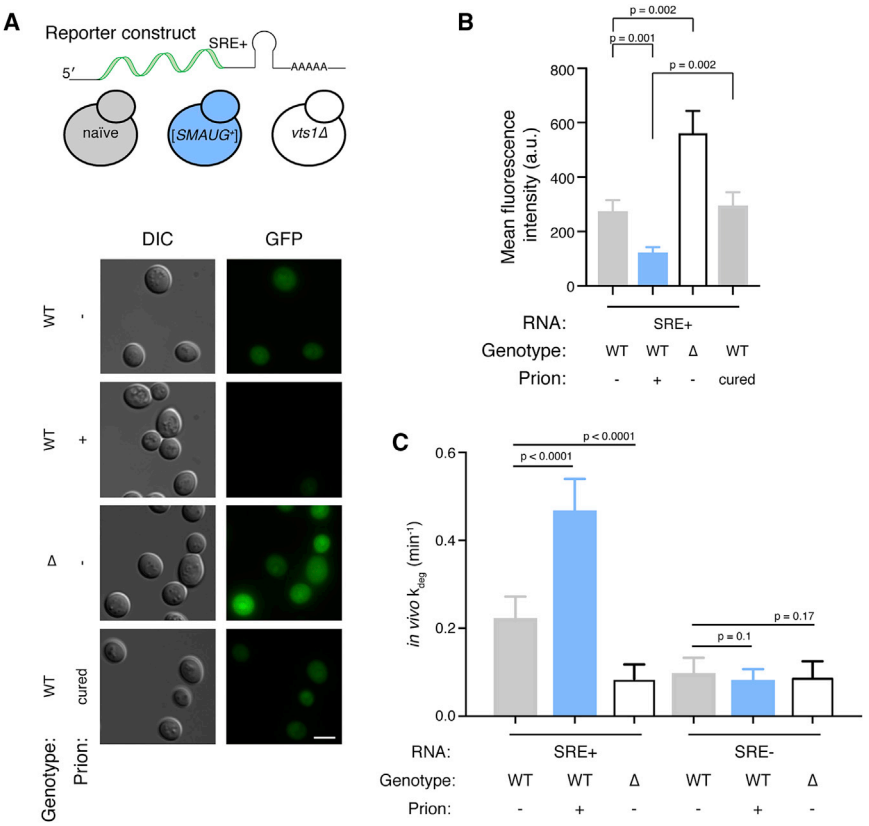

Figure 1. Vts1 Activity Is Enhanced in [*SMAUG*$^+$] Cells

(A) Schematic of GFP-SRE+ reporter and genetic backgrounds used (top). Representative differential interference contrast (DIC) and GFP images of cells expressing the GFP-SRE+ reporter. Scale bar, 5μm.

(B) Quantification of the micrographs. Data are means ± SEM from ~80 individual cells.

(C) *In vivo* apparent degradation rate constants for GFP-SRE+ and GFP-SRE− mRNAs from single exponential fits.

Data are means ± SEM from 3 biological replicates. p values (B and C), Welch's t test.

that are heritable over long biological timescales (Chakrabortee et al., 2016). These traits bore the genetic hallmarks of protein-based inheritance, but many lacked key biochemical features of archetypal prions. Here, we examine an exemplar formed by the evolutionarily ancient RBP Vts1 (Smaug in metazoans).

The Vts1 protein, originally identified in *Drosophila,* is widely conserved across eukaryotes, with orthologs in *S. cerevisiae* and humans (hSmaug1; Aviv et al., 2003, 2006b; Baez and Boccaccio, 2005; Rendl et al., 2008; Smibert et al., 1996). In *Drosophila*, Smaug is a critical regulator of early embryonic development, orchestrating degradation of most maternal transcripts during the maternal-to-zygotic transition (Benoit et al., 2009; Chen et al., 2014; Tadros et al., 2007). Here, we first establish that Vts1 from *S. cerevisiae* forms biomolecular condensates. These condensates are not composed of amyloid; yet, they self-template in a prion-like manner to drive transgenerational epigenetic inheritance. Unlike classic prions, this conformational conversion is readily reversible and enhances Vts1 function. We name this prion [*SMAUG*$^+$] because of its enhanced capacity to initiate destruction of its target transcripts. Engagement of [*SMAUG*$^+$] drives a gene expression program that is adaptive in stressful environments. Remarkably, the human Vts1 homolog hSmaug1 retains the self-templating capacity. In the adjoining study, we describe how [*SMAUG*$^+$] controls key developmental decisions in *S. cerevisiae* and demonstrate that it occurs pervasively in nearly all laboratory strains and many wild isolates of this organism. Together, our data provide a striking example how self-assembly of intrinsically disordered RBPs can heritably modulate the landscape of post-transcriptional gene control, altering cellular decision-making.

RESULTS

Prion Acquisition Hyperactivates Vts1

We previously found that transient Vts1 overexpression induced a stable phenotype (sensitivity to UV irradiation) with defining characteristics of yeast prions: non-Mendelian inheritance patterns and strong dependence on chaperone activity for transmission (Chakrabortee et al., 2016). Here, using an established reporter construct (Aviv et al., 2003), we examined how this prion affects Vts1 function. Vts1 binds RNA hairpins known as Smaug recognition elements (SREs) in a sequence- and structure-specific manner, initiating their degradation (Aviv et al., 2006b; Johnson and Donaldson, 2006; Oberstrass et al., 2006; She et al., 2017). The reporter we used expresses an inducible GFP fused to a 3′-UTR containing SREs (Aviv et al., 2003) to assess Vts1 function. As a control, we introduced this GFP-SRE+ reporter into isogenic cells that lack the prion (wild-type [WT]-naive) and into cells in which genes encoding Vts1 had been deleted (*vts1Δ*; Figure 1A). We then expressed the reporter and measured the levels of GFP fluorescence. As expected, *vts1Δ* cells were brighter than the WT-naive cells (~2-fold, p = 0.002, Welch's t test; Figures 1A and 1B). In contrast to what would be expected for a loss-of-function aggregate, cells harboring the prion were significantly darker than WT-naive cells (~2.2-fold, p = 0.001, Welch's t test; Figures 1A and 1B) despite expressing Vts1 at similar levels (Figures S1A and S1B). Based on this enhanced degradation phenotype, we hereafter refer to this prion as [*SMAUG*$^+$].

To confirm that reduction in GFP fluorescence arose from prion acquisition, we examined its inheritance patterns. Because prion-based traits rely on molecular chaperones for transmission (Chernoff et al., 1995; Garcia and Jarosz, 2014; Patino et al., 1996; Song et al., 2005; Tapia and Koshland, 2014; Wickner et al., 2004), their inheritance can be permanently abolished by transient chaperone inhibition (Chakrabortee et al., 2016; Cox

et al., 1980; Eaglestone et al., 2000; Jung and Masison, 2001; Wickner, 1994; Wickner et al., 2006). We transformed [*SMAUG*$^+$] cells with a plasmid expressing a dominant-negative Hsp70 mutant (*ssa1*^{K69M}) and propagated them for ~50 generations on selective medium. We then eliminated the plasmid, returned the cells to normal medium, propagated them for an additional 25 generations, and examined their GFP fluorescence. Originally, [*SMAUG*$^+$] cells treated in this way became far brighter (~2.4-fold, $p = 0.002$, Welch's t test; Figures 1A and 1B). That is, transient inhibition of Hsp70 permanently eliminated the [*SMAUG*$^+$] trait.

To examine this phenotype further, we analyzed *GFP-SRE+* transcript levels in a pulse-chase experiment. We induced transcription of the *GFP-SRE+* reporter RNA in both [*SMAUG*$^+$] cells and isogenic naive controls with galactose for 20 min. We then arrested transcription by adding excess glucose, measuring *GFP* transcript levels by qRT-PCR over a 20-min period. We observed 3-fold slower decay of this reporter in *vts1Δ* cells than that in WT controls, consistent with the established specificity of this RBP (Figure 1C). The *GFP-SRE+* transcript was degraded approximately two times faster in [*SMAUG*$^+$] cells than in isogenic naive cells (2.1-fold, $p < 0.0001$, Welch's t test). A *GFP-SRE−* transcript, in which the SRE elements have been permuted to remove critical recognition features, was degraded at equivalent rates in all backgrounds, establishing specificity (Figure 1C). Our findings establish that [*SMAUG*$^+$] is not a loss-of-function state, like many classic yeast prions, but instead enhances the degradation of target transcripts.

Intrinsic Disorder Drives Vts1 Oligomerization

To investigate the mechanism of Vts1 hyperactivation in [*SMAUG*$^+$] cells, we undertook a biochemical approach. Vts1 and its homologs harbor a short, ordered RNA-binding domain (RBD; Aviv et al., 2003, 2006a). Each homolog also contains a very large IDR. This domain architecture has been conserved over hundreds of millions of years, even though the amino acid sequence of the IDRs has diverged significantly (Figures 2A and S2A). Yet, all biochemical studies of Vts1 and its homologs to date have used its RBD alone.

We and others have found that IDRs can drive prion-like phenotypes (Chakrabortee et al., 2016; Toombs et al., 2010). We therefore purified full-length Vts1, its ordered RBD (RBD-Vts1), and its IDR (IDR-Vts1) by using constructs that included a C-terminal SNAP tag, enabling site-specific labeling with a fluorophore (Juillerat et al., 2003). We used an N-terminal poly-histidine affinity tag for initial affinity purification and then removed it proteolytically. We purified these proteins to homogeneity (Figures 2B, 2C, and S2B) and confirmed that full-length Vts1 and RBD-Vts1 could bind RNAs harboring SREs (Figure 2D).

We next investigated the quarternary structure of full-length Vts1. The protein eluted as a dominant single peak on a gel filtration column with a retention volume inconsistent with a monomeric conformation, instead matching the expectation for a hexamer (~489 kDa). This peak also had a small shoulder (~10%) composed of oligomeric species with 8 or more monomers (Figures 2C, S2C, and S2D). IDR-Vts1 also eluted as a dominant single peak with a similar retention volume (Figure 2C). By contrast, RBD-Vts1 eluted as a pure monomer under identical buffer conditions (Figures 2C and S2D). We conclude that the IDR of Vts1 promotes self-association.

Vts1 Forms High-Order Condensates

Proteins mature in an extremely crowded intracellular environment (Tokuriki et al., 2004; van den Berg et al., 2000). To approximate this effect, we utilized a widely used molecular crowder (poly-ethylene glycol MW 8000, hereafter crowder; Alberti et al., 2018; Kuznetsova et al., 2014). Introduction of crowder led to the formation of Vts1 condensates that were visible with a fluorescence microscope within 30 min (Figure 2E). These condensates could be readily separated from unassembled protein on an agarose gel (Figure S2E). Other molecular crowders had similar effects (Figure S2F). Neither RBD-Vts1 nor the SNAP tag formed condensates under identical reaction conditions, even after 24-h incubations (Figure 2E). However, IDR-Vts1 did form condensates (Figure 2E). We conclude that the disordered region of Vts1 is both necessary and sufficient for this assembly.

Vts1 condensates formed at near basal physiological protein concentrations (~150 nM; Figures 2F and S2G; see Supplemental Information for discussion of the relationship between concentration and size; Ghaemmaghami et al., 2003). BSA, used as a control protein of comparable molecular weight, did not form condensates under these conditions (Figure S2H). Purified full-length Vts1 without a SNAP tag also formed condensates robustly (Figure S2H), establishing that the behavior is not an artifact of the tag.

The Vts1 condensates were round, akin to liquid condensates that have been described for some RBPs (reviewed in Alberti, 2017). However, they differed substantially from such structures in at least two important respects. First, the condensates did not fuse into larger round structures over time but, instead, amalgamated into larger (~10 μm) ensembles (Figure 2F). Second, fluorescence recovery after photobleaching (FRAP) revealed that Vts1 within condensates did not readily exchange with protein in solution (Figure 3A). By contrast, proteins in liquid condensates exchange rapidly (Alberti, 2017; Brangwynne et al., 2009; Patel et al., 2015). Thus, the IDR in Vts1 that promotes its self-association into oligomers also endows it with the ability to form gel-like condensates.

Vts1 Condensates Are Not Amyloid

The best-known prions form amyloid fibers (Glover et al., 1997; Liebman and Chernoff, 2012; Prusiner et al., 1983), but we and others previously showed that some do not (Brown and Lindquist, 2009; Chakrabortee et al., 2016). We, therefore, investigated the physicochemical properties of Vts1 condensates. A defining feature of amyloid fibers is resistance to ionic detergents, such as SDS. However, Vts1 condensates were rapidly dissolved by low concentrations of SDS (0.1%, ~30 min; Figures 3B and S3A) and the cationic detergent cetyl trimethyl ammonium bromide (Figure S3B). Incubation with 20-fold lower concentrations of SDS also disrupted the large ensembles into smaller condensates (Figure 3B). In comparison, amyloid prions are resistant to 2% SDS (Kryndushkin et al., 2003).

Finally, we examined the structure of Vts1 condensates by using negative stain transmission electron microscopy. Even at physiological concentrations, the condensates were apparent

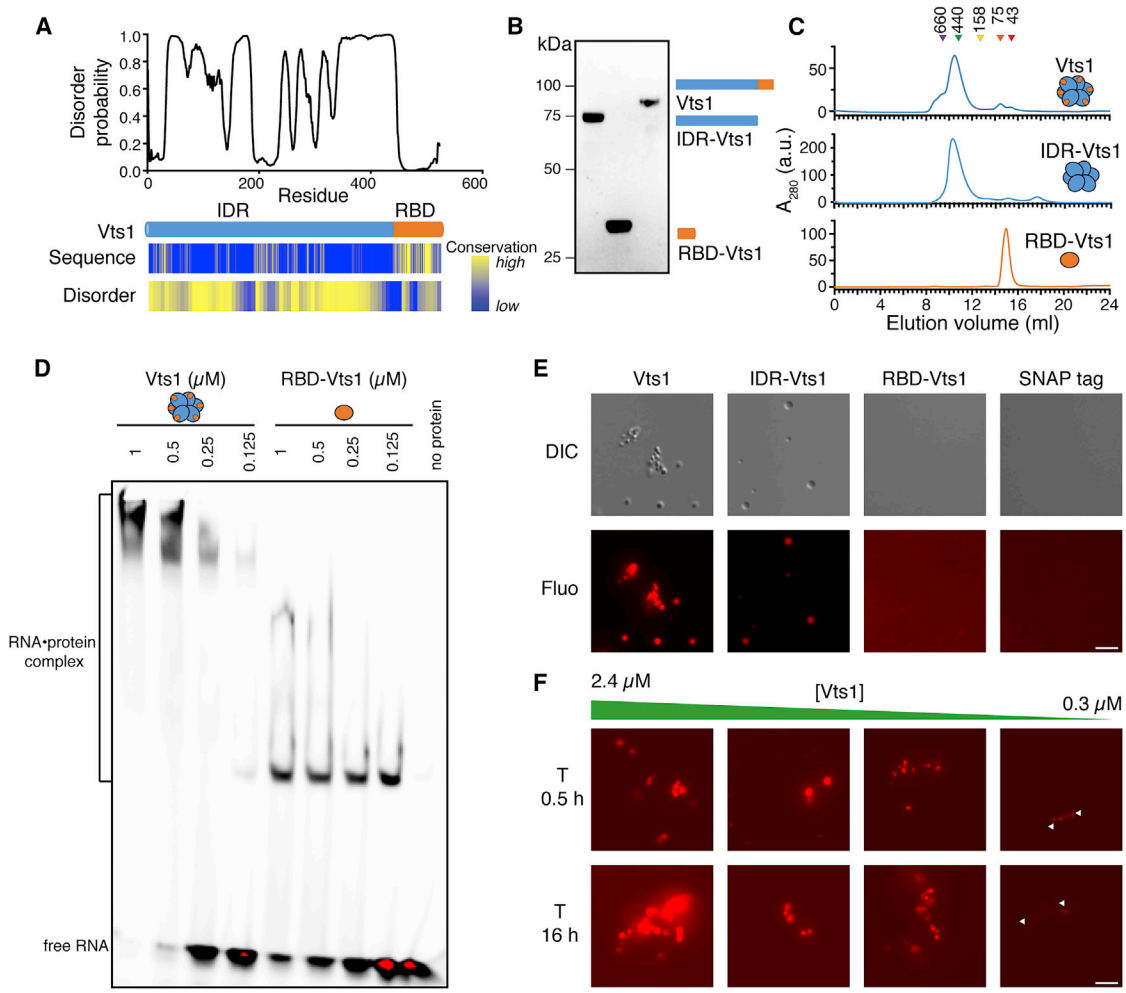

Figure 2. IDR in Vts1 Drives Formation of Condensates

(A) Disorder probability plot of *S. cerevisiae* Vts1 and its domain architecture. Sequence and disorder conservation across 20 fungal species separated by ~200 million years of evolution.

(B) Coomassie-stained SDS-PAGE gel of IDR-Vts1, RBD-Vts1, and Vts1.

(C) Size exclusion chromatography traces of Vts1, IDR-Vts1, and RBD-Vts1. Arrowheads indicate standards and their molecular weight (MW) (in kDa): thyroglobulin (purple), ferritin (green), aldolase (yellow), conalbumin (orange), and ovalbumin (red).

(D) Electrophoretic mobility shift assay (EMSA) of fluorescein-labeled SRE+ RNA with Vts1 and RBD-Vts1.

(E) Representative images of labeled Vts1, IDR-Vts1, RBD-Vts1, and SNAP tag alone in presence of crowder in DIC and SNAP^{549} channels. Scale bar, 5 μm.

(F) Effect of concentration and time on Vts1 condensates. Scale bar, 5 μm.

as electron-dense structures (Figure S3C). None resembled a fibril (Figures S3C and S3D), in contrast to rod-like structures formed by the NM (N-terminal and middle) domain of the well-characterized amyloid prion Sup35. Moreover, Vts1 condensates did not stain with the amyloid binding dye Thioflavin-T (Figure S3E). Based on these observations, the Vts1 condensates are unlikely to be composed of amyloid fibers.

Vts1 Particles Have Prion-like Properties

Altered proteolytic digestion and the capacity to self-template are hallmark biochemical properties of prions (Castilla et al., 2005; Glover et al., 1997; McKinley et al., 1983; Paushkin et al., 1997). We tested whether Vts1 condensates shared these features. We first incubated Vts1 condensates with proteinase K, finding that they were significantly more resistant to proteolytic degradation than unassembled protein (Figures S3F and S3G). We further tested whether the condensates could seed new rounds of assembly—the basis of prion propagation. We generated green- and red-labeled Vts1 by conjugating SNAP-Surface^{488} or SNAP-Surface^{549} dyes. Next, we added crowder to red-Vts1 to create condensates. We then tested whether naive green-Vts1 could form condensates, in the absence of additional crowder, when seeded (<20% v/v) with assembled red-Vts1. We observed robust assembly of green-Vts1 in these experiments, including co-assembly of the green- and red-labeled protein (Figures 3C and S3H). In buffer-matched control experiments, we observed no condensate formation. Although red-Vts1 was typically brighter than green-Vts1, there was no detectable

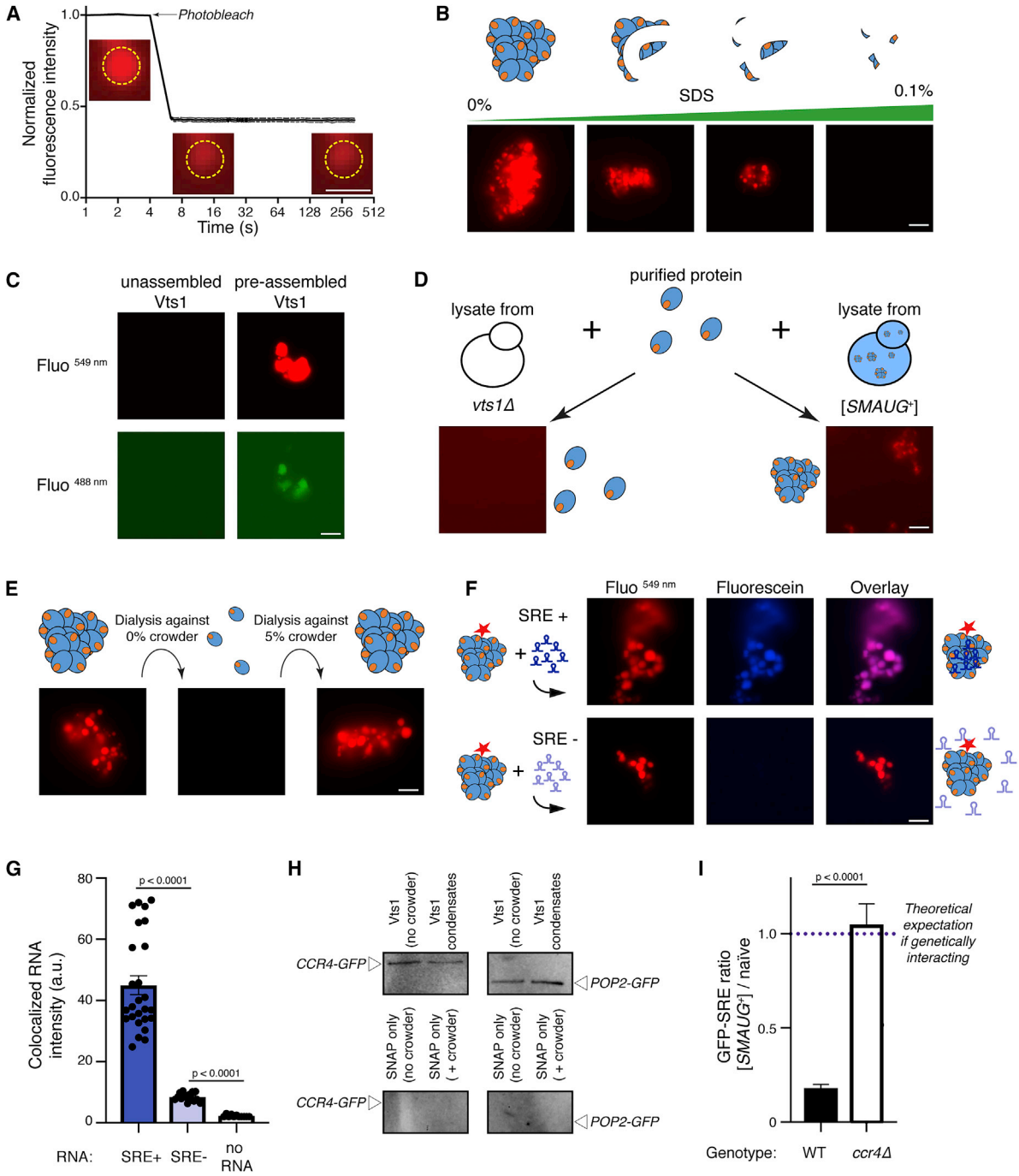

Figure 3. Properties of Vts1 Condensates

(A) FRAP curve of labeled Vts1 condensates. Trace depicts means ± SEM of 3 individual experiments. Insets show FRAP status at indicated times. Yellow dotted circle marks photobleached area. Scale bar, 1 μm.

(B) Representative images showing SDS sensitivity of Vts1 condensates.

(C) Seeding of $SNAP^{488}$-labeled Vts1 (green signal) with pre-assembled $SNAP^{549}$-labeled Vts1 (red signal). Buffer-matched controls with unassembled $SNAP^{549}$ labeled Vts1 depicted on the left.

(D) Seeding of Vts1 condensation by cell lysates from indicated yeast strains.

(E) Reversibility of Vts1 condensates.

(F) Vts1 condensates bind RNA. Representative images of Vts1 condensates (in red), SRE+ (top row), and SRE− RNA (bottom row) in blue, and their overlay (in magenta) are shown.

Scale bar (B–F), 5 μm.

(legend continued on next page)

signal bleed-through between the channels (Figure S3I). Thus, despite their non-amyloid nature, Vts1 condensates bear defining biochemical features of prion biology.

To further examine the relationship between Vts1 condensation and [*SMAUG*$^+$], we incubated fluorescently labeled full-length Vts1 in buffer without crowder but containing unlabeled lysate from [*SMAUG*$^+$] yeast cells. As a control, we performed the same experiment by using lysate from naive *vts1Δ* cells. Labeled Vts1 condensates formed readily in the reactions seeded with [*SMAUG*$^+$] lysate (Figure 3D) but not in in reactions seeded with *vts1*Δ lysate. Collectively, our data establish that Vts1 condensates formed *in vitro* and lysates from [*SMAUG*$^+$] cells can self-template.

Vts1 Condensates Are Reversible and Functional

Amyloid prions are remarkably stable. Their fragmentation often requires enzymatic disaggregase activity (Chernoff et al., 1995; Shorter and Lindquist, 2004). However, because Vts1 condensates had distinct biochemical properties, we asked whether reversal of the crowding conditions would have any effect on them. Remarkably, Vts1 condensates were almost entirely eliminated upon removal of crowder (Figure 3E). Re-addition of crowder led to re-generation of condensates. As a control, we examined a previously aggregated Vts1 protein fraction (eluate in the void volume of a size exclusion chromatography experiment). These non-specific aggregates were irreversible (Figure S3J). Elevated temperature (~55°C) also induced non-specific and irreversible Vts1 aggregation (Figure S3K). Thus, reversibility is a unique property of non-amyloid, self-templating Vts1 condensates.

We next investigated whether specific RNA-binding activity was preserved in the non-amyloid Vts1 condensates by incubating them with fluorescently labeled target RNAs containing SREs (SRE+). We observed robust co-localization (Figure 3F). To test the specificity of this binding, we examined an RNA in which two nucleotides within the recognition hairpin were permuted (SRE− ; Aviv et al., 2003). Vts1 condensates bound more strongly to SRE+ RNA than SRE− RNA (>5-fold, $p < 0.0001$ by Welch's t test), establishing they retain selectivity for target sequences (Figures 3F, 3G, and S4A), and mirroring the specificity of enhanced target degradation in [*SMAUG*$^+$] cells (Figure 1C).

We next investigated whether Vts1 condensates could engage the other key aspect of Vts1 function—recruiting deadenylase machinery (CCR4 and POP2). We generated Vts1-SNAP^{Biotin} condensates (Figure S4B), incubated them with lysates from yeast strains harboring CCR4-GFP or POP2-GFP fusions (Figure S4C), and affinity precipitated the condensates with streptavidin beads (Figure S4B). Both Ccr4 and Pop2 were as efficiently co-precipitated by Vts1-SNAP^{Biotin} condensates as by uncondensed Vts1 but SNAP^{Biotin} alone did not (Figure 3H). To test the functional importance of this interaction *in vivo*, we examined whether enhanced degradation of GFP-SRE in [*SMAUG*$^+$] cells required these effectors. We took advantage of cytoduction, a technique that permits cytoplasmic transfer from donor strains into recipients, without the exchange of nuclear material (Figure S4D; details in STAR Methods). In WT recipients, we observed low GFP-SRE fluorescence with [*SMAUG*$^+$] donors, as expected (Figure 3I). In *ccr4Δ* recipients, by contrast, we observed nearly identical GFP levels regardless of whether the donor had [*SMAUG*$^+$] or naive cytoplasm (Figure 3I). Thus, crucial target binding and effector recruitment functions are preserved in Vts1 condensates and [*SMAUG*$^+$].

Vts1 Condensates Generated *In Vitro* Heritably Transform Naive Cells

Could non-amyloid Vts1 condensates generated *in vitro* heritably alter cellular phenotype? To investigate, we used transformation as a gold-standard test (Tanaka et al., 2004). We designed an endogenous [*SMAUG*$^+$] reporter, inserting a *URA3* marker into the *YNR034W-A* locus, which encodes a protein of unknown function and was downregulated in [*SMAUG*$^+$] cells (Figures 4A, S4E, and S4F). Consistent with lower uracil availability, we observed longer lag times in [*SMAUG*$^+$] cells than in naive cells when grown in medium lacking uracil ($p < 0.0007$; Welch's t test; Figures 4A and S4G). Independent [*SMAUG*$^+$] inductants (Chakrabortee et al., 2016) behaved similarly ($p = 0.5476$; Welch's t test; Figures 4A and S4G), establishing the robustness of this reporter.

Next, we grew naive yeast cells harboring the *YNR034W-A::URA3* reporter and digested their cell walls (Figure 4B, top panel). We transformed these spheroplasted cells with Vts1 condensates, including a centromeric *LEU2* carrier plasmid, to score for uptake of extracellular material. In parallel, we performed analogous experiments with BSA as a control. We selected 43 individual LEU+ colonies and passaged them for 100–125 generations on medium lacking leucine, eliminating any original Vts1 condensates by dilution. We then grew these transformants in medium lacking uracil to assess whether they had become [*SMAUG*$^+$].

Over 80% of the LEU+ colonies (35 out of 43) that were co-transformed with Vts1 condensates exhibited a heritable reduction in growth on medium lacking uracil, just as [*SMAUG*$^+$] cells did (Figure 4B). Cells transformed with BSA did not acquire this trait ($p < 0.0001$, Welch's t test). Transformation required a reservoir of Vts1 protein: *vts1Δ* cells were not transformable by Vts1 condensates ($p = 0.4260$, Welch's t test; Figure 4C). We also investigated GFP-SRE fluorescence in the transformants. The mean GFP signal was significantly reduced in cells whose ancestors (~100–125 generations prior) had been transformed with Vts1 condensates. By contrast, GFP signal was unaffected in cells whose ancestors were transformed with BSA ($p = 0.001$, Tukey's multiple t test; Figure S4H). Parallel experiments with a *GFP-SRE−* reporter showed no difference between lineages transformed with Vts1 condensates or BSA ($p = 0.1630$, Tukey's multiple test; Figure S4H). These data establish that Vts1 condensates can transmit [*SMAUG*$^+$] as proteinaceous infectious

(G) Quantification of fluorescein signal co-localized with Vts1 condensates. p value, Welch's t test.

(H) Affinity precipitation of interactors with soluble and condensed Vts1.

(I) Ratio of mean GFP intensity from GFP-SRE+ reporter in [*SMAUG*$^+$]/naive cells in WT and *ccr4Δ* strains. Dotted line marks the theoretical expectation if [*SMAUG*$^+$] and *CCR4* were genetic interactors. p value, Welch's t test.

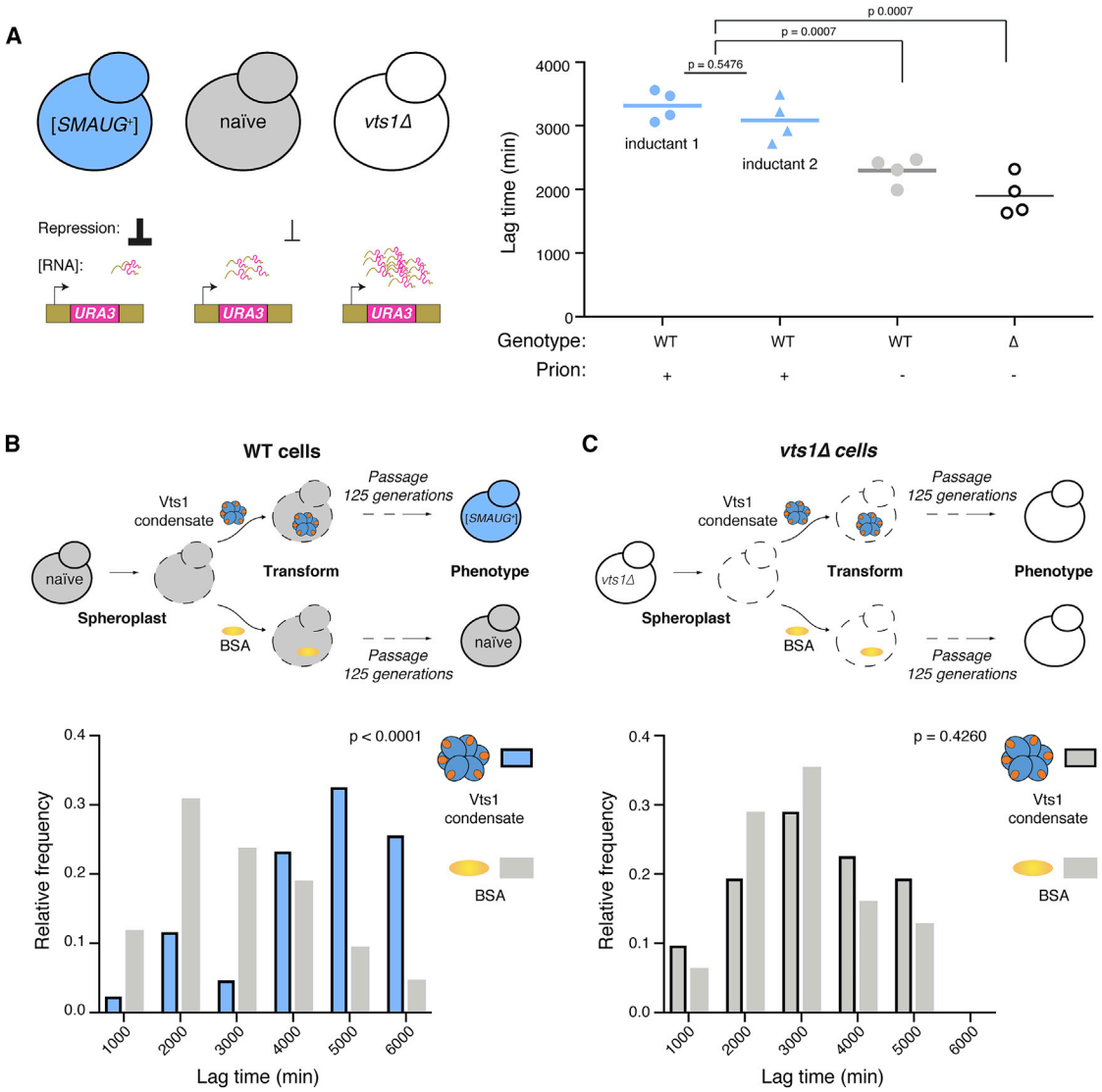

Figure 4. Vts1 Condensates Transform Naive Cells into [*SMAUG*$^+$] Cells

(A) Endogenous reporter used to assay [*SMAUG*$^+$] (left). Lag times of strains with indicated genotype and prion status in medium lacking uracil (right). Bar depicts mean of 4 biological replicates. p value, Welch's t test.

(B and C) Top: schematic of protein transformation in WT-naive (B) and *vts1Δ* cells (C). Bottom: histogram of lag times of individual transformants after incubation with Vts1 condensates (blue bars, black borders in WT-naive; gray bars, black borders in *vts1Δ* cells) or BSA (gray bars in both) in WT-naive (B) and *vts1Δ* cells (C) respectively. p value, Welch's t test.

particles, conforming to the classical definition of a prion (Prusiner, 1982), despite their non-amyloid structure.

A Prion-Based Regulon

We next investigated the consequences of [*SMAUG*$^+$] acquisition transcriptome-wide, performing mRNA sequencing on naive, [*SMAUG*$^+$], and *vts1Δ* cells. More than 80% of the variance among these samples was explained by the first two principal components in a decomposition of the datasets (Figure 5A). Biological replicates (and separate [*SMAUG*$^+$] inductants) clustered closely. The transcriptional profiles of [*SMAUG*$^+$] cells were distant from both naive and *vts1Δ* cells (Figure 5A), supporting the conclusion that [*SMAUG*$^+$] does not abrogate Vts1 function. Rather, this prion engages an alternative gene expression program.

Many mRNAs encoding housekeeping genes were unchanged in naive and [*SMAUG*$^+$] cells. Some studies have previously referred to amyloid prions as diseases (Nakayashiki et al., 2005), in part because cells harboring these elements can upregulate stress-responsive molecular chaperones. Yet, [*SMAUG*$^+$] cells did not upregulate messages encoding heat shock proteins or sentinel stress transcription factors, such as *MSN2/4* or *HSF1* (Table S1). Across the transcriptome, we did observe a clear and reproducible effect of [*SMAUG*$^+$]: downregulation of hundreds of

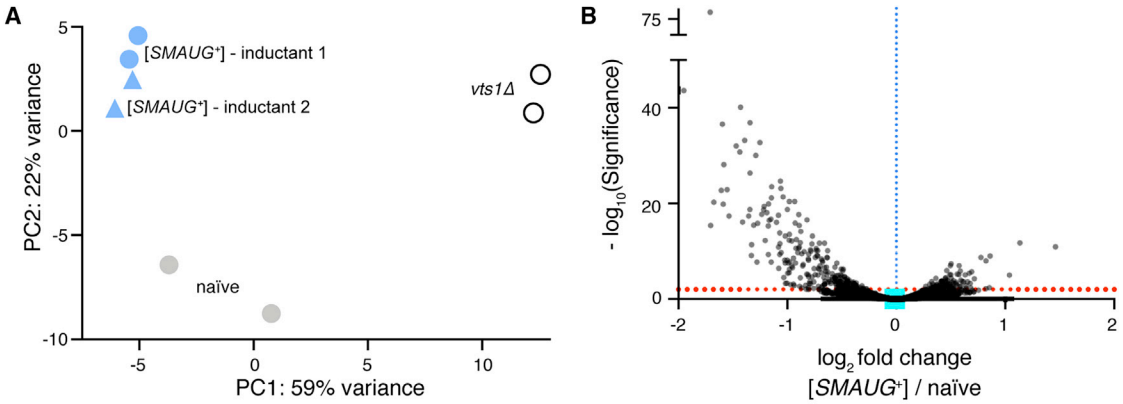

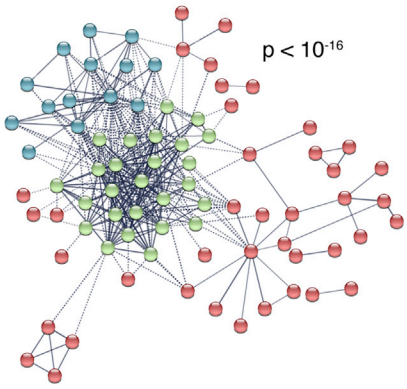

D

Gene Ontology terms	FDR
Carbohydrate transport (11 genes)	5.15×10^{-6}
Energy reserve metabolic processes (9 genes)	5.65×10^{-6}
Glycogen metabolic process (8 genes)	3.22×10^{-5}
Cellular carbohydrate metabolic process (15 genes)	3.22×10^{-5}

Figure 5. [*SMAUG*$^+$] Drives a Prion-Based Regulon

(A) Principal-component analysis (PCA) of biological replicate transcriptomes from naive, two independent [*SMAUG*$^+$] inductants, and *vts1Δ* strains.

(B) Volcano plot of $-\log_{10}$(adjusted p values) versus $\log_2$(fold change) of transcriptome-wide mRNA abundances in [*SMAUG*$^+$] relative to naive cells. The red dotted line indicates the significance cutoff (false discovery rate [FDR] = 1%; Benjamini-Hochberg corrected). Teal square depicts ratio of RNA abundance in [*SMAUG*$^+$] versus naive cells for *ACT1* mRNA.

(C) Network of physical and genetic interactions for transcripts uniquely downregulated in [*SMAUG*$^+$] cells. Target RNAs were clustered by k-means. p value, hypergeometric test.

(D) Top Gene Ontology terms and associated genes that were downregulated in [*SMAUG*$^+$] cells.

transcripts relative to naive cells (189 downregulated versus 44 upregulated transcripts, $p < 10^{-8}$ by binomial test; Figure 5B; Table S1). This was notable because native Vts1 already downregulates the expression of its target transcripts (She et al., 2017).

Downregulated transcripts in [*SMAUG*$^+$] cells overlapped significantly with those stabilized in *vts1Δ* cells ($p < 4.03 \times 10^{-17}$ by hypergeometric test; Figure S5A). We asked if transcripts uniquely downregulated in [*SMAUG*$^+$] cells were identified as targets of Vts1 in transcriptome-wide RNA-binding experiments (Aviv et al., 2006b; Hogan et al., 2008; She et al., 2017). Indeed, many were identified as targets ($p < 7.71 \times 10^{-6}$ by hypergeometric test; Figures S5A and S5B), suggesting that prion-specific changes in gene expression often come from direct binding, consistent with [*SMAUG*$^+$] being a hyperactive form of the protein.

To analyze the functional impact of the [*SMAUG*$^+$] transcriptome, we next investigated the genes downregulated uniquely in cells harboring the prion. Leveraging systematic studies of physical and genetic interactions in *S. cerevisiae*, we assembled downregulated targets (adjusted $p < 0.01$ and $\log_2$-fold change < -0.5) into a network (Szklarczyk et al., 2015). Targets that were downregulated in [*SMAUG*$^+$] cells were far more interconnected than expected by chance ($p < 1.0 \times 10^{-16}$, hypergeometric test; Figure 5C). Sub-networks included a large cluster of genes involved in carbohydrate metabolism, reflected by Gene Ontology (GO) term enrichments for energy reserve metabolic processes (9 genes; $p = 5.15 \times 10^{-6}$) and carbohydrate transport (11 genes; $p = 5.65 \times 10^{-6}$; Figures 5D and S5C). This relationship was especially strong among direct Vts1 targets (Figure S5D). The connectivity and shared function among targets uniquely downregulated in [*SMAUG*$^+$] cells led us to investigate whether the prion engaged a gene expression program that could have adaptive value.

[*SMAUG*$^+$] Provides an Adaptive Advantage

Because transcripts uniquely regulated by [*SMAUG*$^+$] were enriched in carbohydrate metabolism, we tested the capacity of

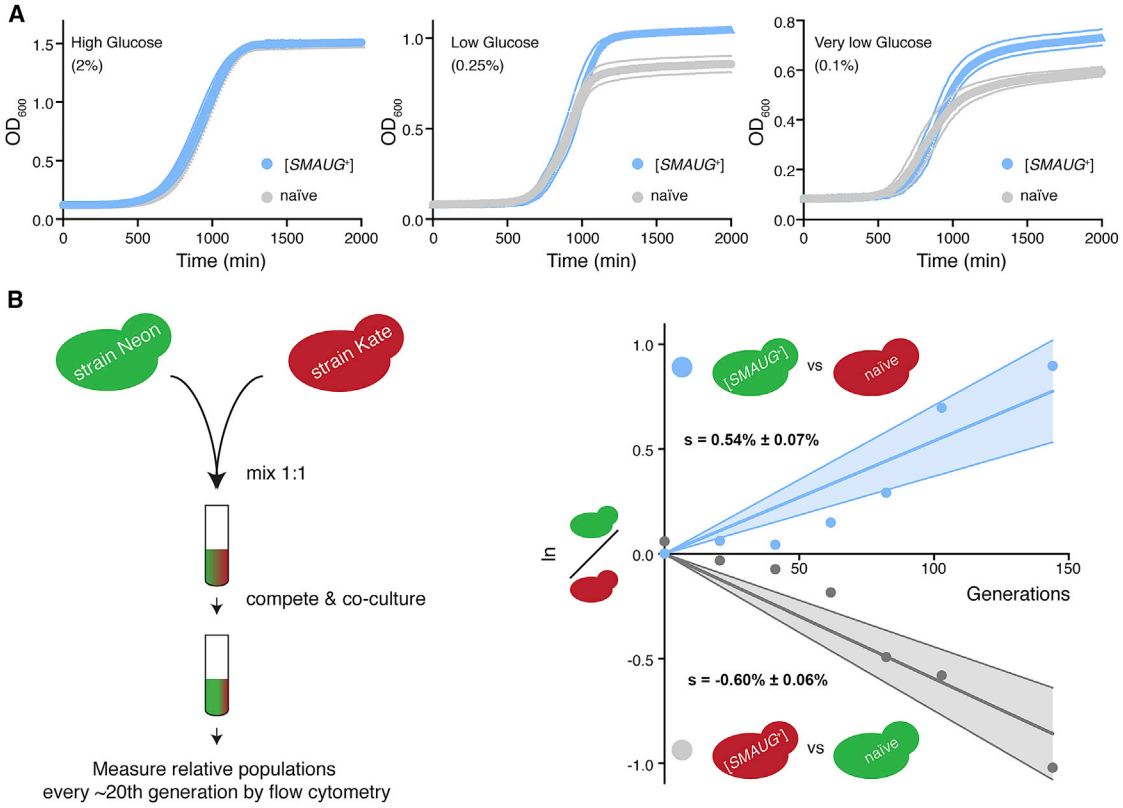

Figure 6. [*SMAUG*$^+$] Provides an Adaptive Advantage

(A) Growth curves for naive and [*SMAUG*$^+$] strains in different glucose concentrations. Each point depicts mean ± SEM of 3 biological replicates.

(B) Competition experiment schematic. Normalized fluorescence intensities (Neon/Kate) when naive and [*SMAUG*$^+$] cells are co-cultured are depicted. Blue plot represents data obtained when [*SMAUG*$^+$] cells were Neon-marked and naive cells were Kate-marked; gray plot represents data from the marker-swap experiment. Blue and gray solid lines depict linear fits of (Neon/Kate) intensities versus time, and the shaded region bounded by dashed lines represents the 95% confidence interval over 3 biological replicates.

[*PRION*$^+$] and [*prion*$^-$] cells to respond to different levels of glucose availability. We observed no effect on either growth rate or carrying capacity (maximum optical density 600 [OD_{600}]) of individual cultures in growth medium containing high glucose (2%; Figure 6A). However, [*SMAUG*$^+$] cells had a clear growth advantage in low glucose (Figure 6A).

Because the average selection coefficients that have driven the fixation of genetic variation are sufficiently small that they require multiple generations of competition to be observed (Concepción-Acevedo et al., 2015; Wilson et al., 2014), we performed a competitive co-culture experiment. We tagged naive and [*SMAUG*$^+$] cells with different fluorescent proteins (mNeonGreen and mKate2) and, starting with equal fractions of each marked cell population, propagated mixed cultures over ~100 generations in standard growth medium. Every 20 generations, we diluted the cultures 200-fold and measured the abundance of each fluorophore by flow cytometry (Figure 6B). Because the expression of fluorescent proteins can affect growth rates (Kafri et al., 2016), we also conducted swapped-color controls. In these experiments WT-[*SMAUG*$^+$] cells also outcompeted naive cells (selection coefficient "s" ~0.6% ± 0.06%; Figure 6B). As a frame of reference, this selection coefficient is larger than that attributed to approximately one-third of all non-essential genes in *S. cerevisiae* (Breslow et al., 2008; Figure S6). Notably, deletion of several key players in the carbohydrate uptake and storage downregulated in [*SMAUG*$^+$] cells (e.g., *GLC3*, *IGD1*, *HXT4*, *PIG2*, and *SPG4*) provides similar fitness advantages (Breslow et al., 2008). These data establish the power of [*SMAUG*$^+$] to fuel robust changes in the post-transcriptional gene expression landscape and corresponding transformations of phenotype.

Self-Templating in Metazoan Smaug Homologs

Despite considerable sequence divergence, Vts1/Smaug homologs across Eukarya harbor a small RBD coupled to large IDRs (Figures 7A and S7A). We investigated whether human Smaug (hSmaug1) was also able to act as a prion by expressing and purifying hSmaug1 and following a similar strategy as we had used for the yeast protein. Purified hSmaug1 (Figure S7B) bound SRE-containing RNAs in electrophoretic mobility shift assays (Figure S7C), confirming its activity. SNAP-surface^{549}-labeled hSmaug1 also robustly assembled into micron scale condensates in the presence of crowder, just as in Vts1 (Figure 7B).

We also examined the capacity of hSmaug1 to form heritable assemblies in cells. We transformed naive yeast cells

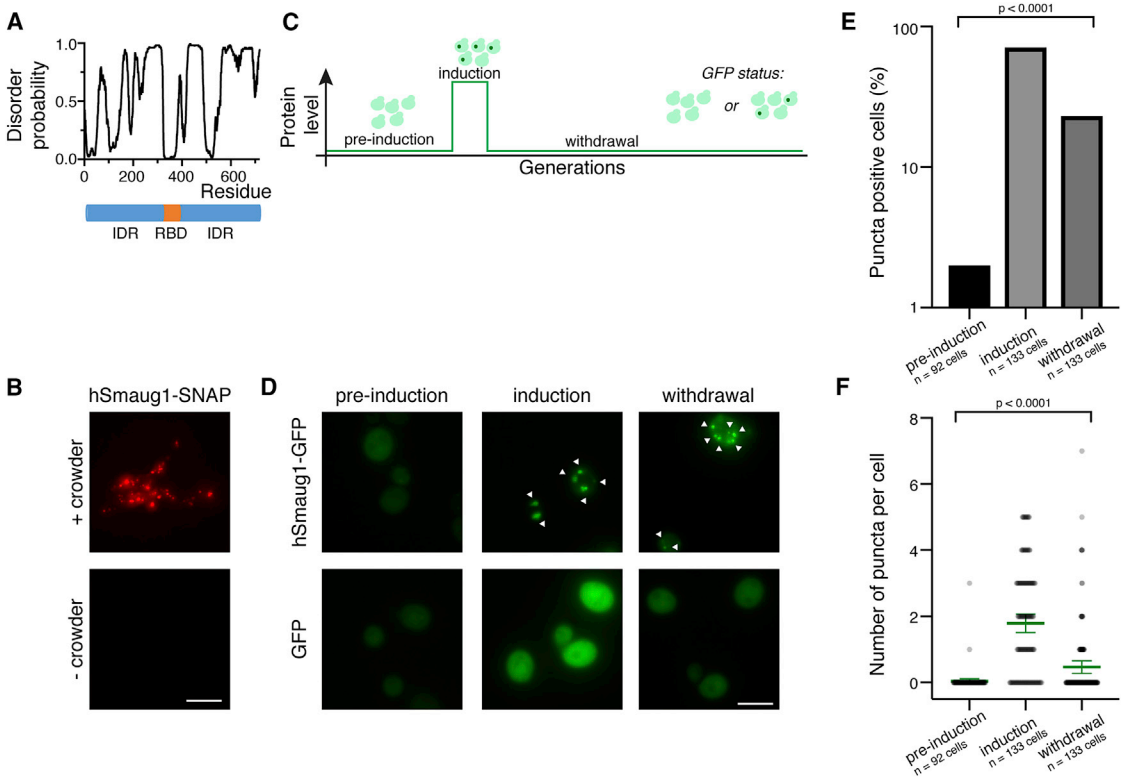

Figure 7. Metazoan Vts1/Smaug Homolog Can Form Condensates and Self-Template

(A) Disorder profile and domain architecture of hSmaug1.

(B) Condensates formed by purified hSmaug1 in presence of crowder.

(C) Transient overexpression experiment schematic.

(D) Representative micrographs of strains harboring GFP-tagged hSmaug1 or GFP alone at different experimental stages. White arrows highlight puncta.

(E and F) Quantification of micrographs from experimental regimen. Plot of percent of cells with puncta; p value represents the statistical significance of difference in pre-induction and withdrawal samples by Fisher's exact test (E). Scatter dot plot of number of puncta per cell; green bars represent mean ± 95% confidence interval of this distribution, p value, Welch's t test (F).

with constructs expressing C-terminally GFP-tagged hSmaug1 controlled by a galactose-inducible promoter. At low levels, hSmaug1-GFP was diffuse. Upon strong induction, it formed bright fluorescent puncta. We next washed these cells and diluted them 400-fold into growth medium that again induced low protein levels. We propagated these cultures for 48 h and examined the distribution of GFP in the resulting daughters (Figure 7C). As a control, we performed identical experiments in cells expressing only GFP. We never observed GFP puncta at any stage of the experiment (Figure 7D). In contrast, hSmaug1-GFP continued to propagate as puncta in daughter cells, despite considerable dilution inherent to the experiment (Figures 7D–7F). We conclude that over very large evolutionary distances Vts1/Smaug homologs have retained the capacity to form self-templating condensates.

DISCUSSION

Prions subvert the central dogma, allowing proteins to transmit information across generations. When nucleic-acid-binding proteins act as prions, they can reshape the primary conduit of information flow within the cell. The amyloid conversion of prion proteins, like Sup35, Mod5, or mammalian PrP^{C}, commonly drives loss of function or toxic gain of function (Prusiner, 1997; Suzuki et al., 2012; Uptain and Lindquist, 2002). Here, we found that [*SMAUG*$^{+}$], a non-amyloid prion formed by the highly conserved RBP Vts1, does neither. Rather, [*SMAUG*$^{+}$] hyperactivates Vts1's capacity to degrade its RNA targets. [*SMAUG*$^{+}$] can be reconstituted *in vivo* by transformation of naive yeast cells with Vts1 condensates made *in vitro*. These gel-like particles are distinct from archetypal amyloid prions and, yet, also self-template robustly. Vts1 condensates are, thus, true prions—proteinaceous and infectious particles—with strong adaptive value.

Vts1's IDR drives its condensation to produce the minimal functional unit of this prion. Phase separation mediated by intrinsically disordered proteins can have diverse mesoscopic properties (Boeynaems et al., 2018). These include droplets that exchange material rapidly with their surroundings (Elbaum-Garfinkle et al., 2015), gel-like condensates (Woodruff et al., 2017), and amyloid fibers (Boke et al., 2016). Vts1 condensates are most comparable to gel-like species, although their heritability distinguishes them. They appear spherical rather than fibrillar but do not coalesce

into a single droplet over time or readily exchange material with their surroundings. Their reversibility suggests that the interactions that drive their formation are likely noncovalent. Alternate high-order assemblies of Vts1, including those generated at high temperature, are not reversible, suggesting that the assembly states of this protein that can transmit epigenetic information are not generic aggregates. Elucidating the specific structural properties that enable self-templating of this and other non-amyloid prions is an exciting avenue for future study.

The potential for phase-separated condensates to spatiotemporally coordinate gene regulation, particularly at the transcriptional level, has recently garnered substantial interest (Boija et al., 2018; Cho et al., 2018; Sabari et al., 2018). Protein phase separation impacts diverse aspects of biology, including anteroposterior axis formation in *Caenorhabditis elegans* (Brangwynne et al., 2009; Smith et al., 2016), gene silencing by heterochromatin in flies and human cells (Larson et al., 2017; Strom et al., 2017), and ribonucleoprotein granule formation in budding yeast. The latter can occur under stress, after deceptive encounters during courtship, and in mediating translational repression during meiosis (Berchowitz et al., 2015; Caudron and Barral, 2013; Riback et al., 2017). However, these condensates are either formed and dissolved over the course of a cell cycle (e.g., Cdc19 aggregates; Saad et al., 2017), destroyed during development (e.g., the Balbiani body; Boke et al., 2016), or retained in mother cells (e.g., Whi3 super-assemblies; Caudron and Barral, 2013). By contrast, Vts1 condensates drive traits that are inherited over hundreds of generations, through both mitotic and meiotic cell divisions. These proteinaceous particles, thus, integrate certain properties of phase separation with other features of prion-based feedback to provide a robust mechanism for the inheritance of biological traits.

The conserved Hsp70 machinery is paramount in mediating this form of inheritance. Many RBPs contain IDRs that resemble those in Vts1. Many of these have also emerged as non-amyloid prion candidates that depend on Hsp70 (Chakrabortee et al., 2016) rather than Hsp104 disaggregase for their inheritance (as classic amyloid prions do). Hsp70 homologs are ubiquitous throughout life, whereas Hsp104 is absent from animals (Shorter, 2008). Intrinsic links between environmental perturbations and Hsp70 chaperone activity (reviewed in Rosenzweig et al., 2019) also provide potential mechanisms for regulating the acquisition (and loss) of these epigenetic states.

Amyloid prions like [*PSI*$^+$], [*MOD*$^+$], [URE3], and [*SWI*$^+$] often phenocopy a deletion of their causal proteins. In the prion state, these proteins are sequestered into fibrillar aggregates, leading to losses of function (Baxa et al., 2002; Chernoff et al., 1995; Du et al., 2015; Suzuki et al., 2012). Extending the palette of protein-based traits, [*SMAUG*$^+$] does the opposite, hyperactivating the native protein's ability to downregulate its targets. Metazoan orthologs of Vts1 can also function in translational repression (Baez and Boccaccio, 2005; Chen et al., 2014; Jeske et al., 2011; Niu et al., 2017; Smibert et al., 1996), and the potential contribution of [*SMAUG*$^+$] at both post-transcriptional and translational levels in these systems presents an intriguing question for further exploration.

The transcriptome of [*SMAUG*$^+$] cells bears no signature of a stress response. Rather, the robust interconnectivity of downregulated transcripts in these cells defines a prion-based regulatory network enriched in key players in carbohydrate metabolism and storage, including glycogen and trehalose biosynthesis. These two carbohydrates are primary stores of glucose in *S. cerevisiae* (François and Parrou, 2001), providing a logical link between the post-transcriptional effects of [*SMAUG*$^+$] and enhanced proliferation. In the adjoining manuscript (Itakura et al., 2019), we discuss the adaptive impact of [*SMAUG*$^+$] on choice between mitotic versus meiotic developmental programs. We report that distinct [*SMAUG*$^+$] variants are naturally present in diverse yeast populations, sparking allelic diversification of phenotypes linked to this prion. The mechanisms that give rise to this behavior remain to be investigated. One possibility is conformational polymorphism of Vts1 condensates themselves. [*SMAUG*$^+$] variants could also arise from altered interactions in the context of a larger prion complex. Several components of the deadenylation machinery harbor large IDRs that resemble those in Vts1, making them potential candidates for such a complex. It is remarkable that heritable changes in such a fundamental biological phenotype can be driven not by a genetic mutation but rather by a heritably altered protein conformation.

Roughly 50% of human RBPs are substantially disordered (Castello et al., 2016). The ability of [*SMAUG*$^+$] to memorize a burst of protein expression and rewire the transcriptome for many generations thereafter raises intriguing questions regarding RBP function, given the prevalence of disordered sequences within this class of proteins. hSmaug1 retains the self-templating potential despite considerable sequence divergence and also forms foci in hippocampal neurons (Baez and Boccaccio, 2005; Baez et al., 2011). Our data suggest that intrinsic disorder within Vts1/Smaug protein endow it with the capacity to self-assemble into condensates. This drives an extreme form of feedback, creating a conformational memory that outlasts the individual molecules that form such assemblies. The widespread presence of intrinsically disordered sequences in RBPs, thus, offers immense potential for functional diversification over long biological timescales. Yet, aggregation of RBPs, such as hnRNP and FUS, potentially by maturation of phase-separated liquids or gels into toxic aggregates (Lin et al., 2015; Molliex et al., 2015; Patel et al., 2015), can also have devastating consequences for human health. Indeed, Smaug itself is overexpressed in chronic lymphocytic leukemia (Haslinger et al., 2004), and RBPs are commonly overexpressed in human cancers (Kechavarzi and Janga, 2014). It remains to be seen whether the bursts of protein expression inherent to these scenarios also drive heritable self-assembly. Here, we have shown that this behavior can also have profound adaptive value, heritably engaging a coherent gene expression program that drives mitotic proliferation. Collectively, our findings expand the functional versatility of intrinsically disordered sequences, integrating phase separation and bona fide prion activity to heritably transform post-transcriptional gene regulation.

STAR★METHODS

Detailed methods are provided in the online version of this paper and include the following:

- KEY RESOURCES TABLE
- LEAD CONTACT AND MATERIALS AVAILABILITY

SUPPLEMENTAL INFORMATION

Supplemental Information can be found online at https://doi.org/10.1016/j.molcel.2019.10.028.

ACKNOWLEDGMENTS

We are grateful to C. Smibert, K. Frederick, R. Halfmann, M. Khalil, S. Shuman, C. Lima, S. Boeynaems, K. Leppek, L. Xie, C.M. Jakobson, Z. Harvey, and members of the Jarosz laboratory for materials, discussions, and/or critical reading of the manuscript. S. Larios provided critical lab support. Flow cytometry was done at the Stanford Shared FACS Facility and electron microscopy at the Stanford EM core (ARRA award number 1S10RR026780-01 from the National Center for Research Resources). A.K.C. was supported as a Howard Hughes Medical Institute fellow of the Damon Runyon Cancer Research Foundation (DRG2221-15) and by an NIH Pathway to independence award (1K99GM128180-01). This work was supported by NIH grant DP2-GM119140 (to D.F.J.). D.F.J. was also supported as a Searle Scholar, as a Kimmel Scholar, as a Vallee Scholar, by a Science and Engineering Fellowship from the David and Lucile Packard Foundation, and by a CAREER Award (1453762) from the National Science Foundation (NSF).

AUTHOR CONTRIBUTIONS

A.K.C. and D.F.J. conceived and designed research; A.K.C., T.S., and A.K.I. performed experiments; D.M.G. contributed new reagents; A.K.C. analyzed data; and A.K.C. and D.F.J. wrote the paper.

DECLARATION OF INTERESTS

The authors declare no conflict of interest.

Received: April 1, 2019
Revised: August 29, 2019
Accepted: October 17, 2019
Published: November 19, 2019

REFERENCES

Aigle, M., and Lacroute, F. (1975). Genetical aspects of [URE3], a non-mitochondrial, cytoplasmically inherited mutation in yeast. Mol. Gen. Genet. *136*, 327–335.

Alberti, S. (2017). Phase separation in biology. Curr. Biol. *27*, R1097–R1102.

Alberti, S., Gitler, A.D., and Lindquist, S. (2007). A suite of Gateway cloning vectors for high-throughput genetic analysis in Saccharomyces cerevisiae. Yeast *24*, 913–919.

Alberti, S., Halfmann, R., King, O., Kapila, A., and Lindquist, S. (2009). A systematic survey identifies prions and illuminates sequence features of prionogenic proteins. Cell *137*, 146–158.

Alberti, S., Saha, S., Woodruff, J.B., Franzmann, T.M., Wang, J., and Hyman, A.A. (2018). A User's Guide for Phase Separation Assays with Purified Proteins. J. Mol. Biol. *430*, 4806–4820.

Aviv, T., Lin, Z., Lau, S., Rendl, L.M., Sicheri, F., and Smibert, C.A. (2003). The RNA-binding SAM domain of Smaug defines a new family of post-transcriptional regulators. Nat. Struct. Biol. *10*, 614–621.

Aviv, T., Amborski, A.N., Zhao, X.S., Kwan, J.J., Johnson, P.E., Sicheri, F., and Donaldson, L.W. (2006a). The NMR and X-ray structures of the *Saccharomyces cerevisiae* Vts1 SAM domain define a surface for the recognition of RNA hairpins. J. Mol. Biol. *356*, 274–279.

Aviv, T., Lin, Z., Ben-Ari, G., Smibert, C.A., and Sicheri, F. (2006b). Sequence-specific recognition of RNA hairpins by the SAM domain of Vts1p. Nat. Struct. Mol. Biol. *13*, 168–176.

Baez, M.V., and Boccaccio, G.L. (2005). Mammalian Smaug is a translational repressor that forms cytoplasmic foci similar to stress granules. J. Biol. Chem. *280*, 43131–43140.

Baez, M.V., Luchelli, L., Maschi, D., Habif, M., Pascual, M., Thomas, M.G., and Boccaccio, G.L. (2011). Smaug1 mRNA-silencing foci respond to NMDA and modulate synapse formation. J. Cell Biol. *195*, 1141–1157.

Banani, S.F., Lee, H.O., Hyman, A.A., and Rosen, M.K. (2017). Biomolecular condensates: organizers of cellular biochemistry. Nat. Rev. Mol. Cell Biol. *18*, 285–298.

Banjade, S., and Rosen, M.K. (2014). Phase transitions of multivalent proteins can promote clustering of membrane receptors. eLife *3*, e04123.

Bartel, D.P. (2009). MicroRNAs: target recognition and regulatory functions. Cell *136*, 215–233.

Baxa, U., Speransky, V., Steven, A.C., and Wickner, R.B. (2002). Mechanism of inactivation on prion conversion of the Saccharomyces cerevisiae Ure2 protein. Proc. Natl. Acad. Sci. USA *99*, 5253–5260.

Benoit, B., He, C.H., Zhang, F., Votruba, S.M., Tadros, W., Westwood, J.T., Smibert, C.A., Lipshitz, H.D., and Theurkauf, W.E. (2009). An essential role for the RNA-binding protein Smaug during the Drosophila maternal-to-zygotic transition. Development *136*, 923–932.

Berchowitz, L.E., Kabachinski, G., Walker, M.R., Carlile, T.M., Gilbert, W.V., Schwartz, T.U., and Amon, A. (2015). Regulated Formation of an Amyloid-like Translational Repressor Governs Gametogenesis. Cell *163*, 406–418.

Boeynaems, S., Alberti, S., Fawzi, N.L., Mittag, T., Polymenidou, M., Rousseau, F., Schymkowitz, J., Shorter, J., Wolozin, B., Van Den Bosch, L., et al. (2018). Protein Phase Separation: A New Phase in Cell Biology. Trends Cell Biol. *28*, 420–435.

Boija, A., Klein, I.A., Sabari, B.R., Dall'Agnese, A., Coffey, E.L., Zamudio, A.V., Li, C.H., Shrinivas, K., Manteiga, J.C., Hannett, N.M., et al. (2018). Transcription Factors Activate Genes through the Phase-Separation Capacity of Their Activation Domains. Cell *175*, 1842–1855.e1816.

Boke, E., Ruer, M., Wühr, M., Coughlin, M., Lemaitre, R., Gygi, S.P., Alberti, S., Drechsel, D., Hyman, A.A., and Mitchison, T.J. (2016). Amyloid-like Self-Assembly of a Cellular Compartment. Cell *166*, 637–650.

Brangwynne, C.P. (2013). Phase transitions and size scaling of membrane-less organelles. J. Cell Biol. *203*, 875–881.

Brangwynne, C.P., Eckmann, C.R., Courson, D.S., Rybarska, A., Hoege, C., Gharakhani, J., Jülicher, F., and Hyman, A.A. (2009). Germline P granules are liquid droplets that localize by controlled dissolution/condensation. Science *324*, 1729–1732.

Bray, N.L., Pimentel, H., Melsted, P., and Pachter, L. (2016). Near-optimal probabilistic RNA-seq quantification. Nat. Biotechnol. *34*, 525–527.

Breslow, D.K., Cameron, D.M., Collins, S.R., Schuldiner, M., Stewart-Ornstein, J., Newman, H.W., Braun, S., Madhani, H.D., Krogan, N.J., and Weissman, J.S. (2008). A comprehensive strategy enabling high-resolution functional analysis of the yeast genome. Nat. Methods *5*, 711–718.

Brown, J.C., and Lindquist, S. (2009). A heritable switch in carbon source utilization driven by an unusual yeast prion. Genes Dev. *23*, 2320–2332.

Byers, J.S., and Jarosz, D.F. (2014). Pernicious pathogens or expedient elements of inheritance: the significance of yeast prions. PLoS Pathog. *10*, e1003992.

Byrne, K.P., and Wolfe, K.H. (2005). The Yeast Gene Order Browser: combining curated homology and syntenic context reveals gene fate in polyploid species. Genome Res. *15*, 1456–1461.

Calabretta, S., and Richard, S. (2015). Emerging Roles of Disordered Sequences in RNA-Binding Proteins. Trends Biochem. Sci. *40*, 662–672.

Campbell, Z.T., and Wickens, M. (2015). Probing RNA-protein networks: biochemistry meets genomics. Trends Biochem. Sci. *40*, 157–164.

Castello, A., Fischer, B., Eichelbaum, K., Horos, R., Beckmann, B.M., Strein, C., Davey, N.E., Humphreys, D.T., Preiss, T., Steinmetz, L.M., et al. (2012). Insights into RNA biology from an atlas of mammalian mRNA-binding proteins. Cell *149*, 1393–1406.

Castello, A., Fischer, B., Frese, C.K., Horos, R., Alleaume, A.M., Foehr, S., Curk, T., Krijgsveld, J., and Hentze, M.W. (2016). Comprehensive Identification of RNA-Binding Domains in Human Cells. Mol. Cell *63*, 696–710.

Castilla, J., Saá, P., Hetz, C., and Soto, C. (2005). In vitro generation of infectious scrapie prions. Cell *121*, 195–206.

Caudron, F., and Barral, Y. (2013). A super-assembly of Whi3 encodes memory of deceptive encounters by single cells during yeast courtship. Cell *155*, 1244–1257.

Chakrabortee, S., Byers, J.S., Jones, S., Garcia, D.M., Bhullar, B., Chang, A., She, R., Lee, L., Fremin, B., Lindquist, S., et al. (2016). Intrinsically Disordered Proteins Drive Emergence and Inheritance of Biological Traits. Cell *167*, 369–381.e312.

Chakravarty, A.K., and Jarosz, D.F. (2018). More than Just a Phase: Prions at the Crossroads of Epigenetic Inheritance and Evolutionary Change. J. Mol. Biol. *430*, 4607–4618.

Chen, L., Dumelie, J.G., Li, X., Cheng, M.H.K., Yang, Z., Laver, J.D., Siddiqui, N.U., Westwood, J.T., Morris, Q., Lipshitz, H.D., and Smibert, C.A. (2014). Global regulation of mRNA translation and stability in the early Drosophila embryo by the Smaug RNA-binding protein. Genome Biol. *15*, R4.

Chernoff, Y.O., Lindquist, S.L., Ono, B., Inge-Vechtomov, S.G., and Liebman, S.W. (1995). Role of the chaperone protein Hsp104 in propagation of the yeast prion-like factor [psi+]. Science *268*, 880–884.

Cho, W.K., Spille, J.H., Hecht, M., Lee, C., Li, C., Grube, V., and Cisse, I.I. (2018). Mediator and RNA polymerase II clusters associate in transcription-dependent condensates. Science *361*, 412–415.

Collart, M.A., and Oliviero, S. (2001). Preparation of yeast RNA. Curr. Protoc. Mol. Biol. *Chapter 13*, Unit13 12.

Concepción-Acevedo, J., Weiss, H.N., Chaudhry, W.N., and Levin, B.R. (2015). Malthusian Parameters as Estimators of the Fitness of Microbes: A Cautionary Tale about the Low Side of High Throughput. PLoS One *10*, e0126915.

Cox, B.S. (1965). [PSI], a cytoplasmic suppressor of super-suppressors in yeast. Heredity *20*, 505–521.

Cox, B.S., Tuite, M.F., and Mundy, C.J. (1980). Reversion from suppression to nonsuppression in SUQ5 [psi+] strains of yeast: the classificaion of mutations. Genetics *95*, 589–609.

Draper, D.E. (1999). Themes in RNA-protein recognition. J. Mol. Biol. *293*, 255–270.

Du, Z., Zhang, Y., and Li, L. (2015). The Yeast Prion [SWI(+)] Abolishes Multicellular Growth by Triggering Conformational Changes of Multiple Regulators Required for Flocculin Gene Expression. Cell Rep. *13*, 2865–2878.

Eaglestone, S.S., Ruddock, L.W., Cox, B.S., and Tuite, M.F. (2000). Guanidine hydrochloride blocks a critical step in the propagation of the prion-like determinant [PSI(+)] of Saccharomyces cerevisiae. Proc. Natl. Acad. Sci. USA *97*, 240–244.

Elbaum-Garfinkle, S., Kim, Y., Szczepaniak, K., Chen, C.C., Eckmann, C.R., Myong, S., and Brangwynne, C.P. (2015). The disordered P granule protein LAF-1 drives phase separation into droplets with tunable viscosity and dynamics. Proc. Natl. Acad. Sci. USA *112*, 7189–7194.

François, J., and Parrou, J.L. (2001). Reserve carbohydrates metabolism in the yeast Saccharomyces cerevisiae. FEMS Microbiol. Rev. *25*, 125–145.

Franzmann, T.M., Jahnel, M., Pozniakovsky, A., Mahamid, J., Holehouse, A.S., Nüske, E., Richter, D., Baumeister, W., Grill, S.W., Pappu, R.V., et al. (2018). Phase separation of a yeast prion protein promotes cellular fitness. Science *359*, eaao5654.

Frederick, K.K., Michaelis, V.K., Corzilius, B., Ong, T.C., Jacavone, A.C., Griffin, R.G., and Lindquist, S. (2015). Sensitivity-enhanced NMR reveals alterations in protein structure by cellular milieus. Cell *163*, 620–628.

Garcia, D.M., and Jarosz, D.F. (2014). Rebels with a cause: molecular features and physiological consequences of yeast prions. FEMS Yeast Res. *14*, 136–147.

Gerstberger, S., Hafner, M., and Tuschl, T. (2014). A census of human RNA-binding proteins. Nat. Rev. Genet. *15*, 829–845.

Ghaemmaghami, S., Huh, W.K., Bower, K., Howson, R.W., Belle, A., Dephoure, N., O'Shea, E.K., and Weissman, J.S. (2003). Global analysis of protein expression in yeast. Nature *425*, 737–741.

Giaever, G., Chu, A.M., Ni, L., Connelly, C., Riles, L., Véronneau, S., Dow, S., Lucau-Danila, A., Anderson, K., André, B., et al. (2002). Functional profiling of the Saccharomyces cerevisiae genome. Nature *418*, 387–391.

Gietz, D., St Jean, A., Woods, R.A., and Schiestl, R.H. (1992). Improved method for high efficiency transformation of intact yeast cells. Nucleic Acids Res. *20*, 1425.

Glisovic, T., Bachorik, J.L., Yong, J., and Dreyfuss, G. (2008). RNA-binding proteins and post-transcriptional gene regulation. FEBS Lett. *582*, 1977–1986.

Glover, J.R., Kowal, A.S., Schirmer, E.C., Patino, M.M., Liu, J.J., and Lindquist, S. (1997). Self-seeded fibers formed by Sup35, the protein determinant of [PSI+], a heritable prion-like factor of S. cerevisiae. Cell *89*, 811–819.

Griswold, C.K., and Masel, J. (2009). Complex adaptations can drive the evolution of the capacitor [PSI], even with realistic rates of yeast sex. PLoS Genet. *5*, e1000517.

Halfmann, R., Alberti, S., and Lindquist, S. (2010). Prions, protein homeostasis, and phenotypic diversity. Trends Cell Biol. *20*, 125–133.

Harvey, Z.H., Chen, Y., and Jarosz, D.F. (2018). Protein-Based Inheritance: Epigenetics beyond the Chromosome. Mol. Cell *69*, 195–202.

Haslinger, C., Schweifer, N., Stilgenbauer, S., Döhner, H., Lichter, P., Kraut, N., Stratowa, C., and Abseher, R. (2004). Microarray gene expression profiling of B-cell chronic lymphocytic leukemia subgroups defined by genomic aberrations and VH mutation status. J. Clin. Oncol. *22*, 3937–3949.

Heller, R.C., Kang, S., Lam, W.M., Chen, S., Chan, C.S., and Bell, S.P. (2011). Eukaryotic origin-dependent DNA replication in vitro reveals sequential action of DDK and S-CDK kinases. Cell *146*, 80–91.

Hentze, M.W., Castello, A., Schwarzl, T., and Preiss, T. (2018). A brave new world of RNA-binding proteins. Nat. Rev. Mol. Cell Biol. *19*, 327–341.

Hogan, D.J., Riordan, D.P., Gerber, A.P., Herschlag, D., and Brown, P.O. (2008). Diverse RNA-binding proteins interact with functionally related sets of RNAs, suggesting an extensive regulatory system. PLoS Biol. *6*, e255.

Holmes, D.L., Lancaster, A.K., Lindquist, S., and Halfmann, R. (2013). Heritable remodeling of yeast multicellularity by an environmentally responsive prion. Cell *153*, 153–165.

Hyman, A.A., Weber, C.A., and Jülicher, F. (2014). Liquid-liquid phase separation in biology. Annu. Rev. Cell Dev. Biol. *30*, 39–58.

Itakura, A.K., Chakravarty, A.K., Jakobson, C.M., and Jarosz, D.F. (2019). Widespread Prion-Based Control of Growth and Differentiation Strategies in *Saccharomyces cerevisiae*. Mol. Cell *77*. Published online November 19, 2019. https://doi.org/10.1016/j.molcel.2019.10.027.

Jarosz, D.F., and Khurana, V. (2017). Specification of Physiologic and Disease States by Distinct Proteins and Protein Conformations. Cell *171*, 1001–1014.

Jarosz, D.F., Brown, J.C.S., Walker, G.A., Datta, M.S., Ung, W.L., Lancaster, A.K., Rotem, A., Chang, A., Newby, G.A., Weitz, D.A., et al. (2014). Cross-kingdom chemical communication drives a heritable, mutually beneficial prion-based transformation of metabolism. Cell *158*, 1083–1093.

Jeske, M., Moritz, B., Anders, A., and Wahle, E. (2011). Smaug assembles an ATP-dependent stable complex repressing nanos mRNA translation at multiple levels. EMBO J. *30*, 90–103.

Johnson, P.E., and Donaldson, L.W. (2006). RNA recognition by the Vts1p SAM domain. Nat. Struct. Mol. Biol. *13*, 177–178.

Jones, D.T., and Cozzetto, D. (2015). DISOPRED3: precise disordered region predictions with annotated protein-binding activity. Bioinformatics *31*, 857–863.

Juillerat, A., Gronemeyer, T., Keppler, A., Gendreizig, S., Pick, H., Vogel, H., and Johnsson, K. (2003). Directed evolution of O6-alkylguanine-DNA alkyltransferase for efficient labeling of fusion proteins with small molecules in vivo. Chem. Biol. *10*, 313–317.

Jung, G., and Masison, D.C. (2001). Guanidine hydrochloride inhibits Hsp104 activity in vivo: a possible explanation for its effect in curing yeast prions. Curr. Microbiol. *43*, 7–10.

Kafri, M., Metzl-Raz, E., Jona, G., and Barkai, N. (2016). The Cost of Protein Production. Cell Rep. *14*, 22–31.

Kamentsky, L., Jones, T.R., Fraser, A., Bray, M.A., Logan, D.J., Madden, K.L., Ljosa, V., Rueden, C., Eliceiri, K.W., and Carpenter, A.E. (2011). Improved structure, function and compatibility for CellProfiler: modular high-throughput image analysis software. Bioinformatics *27*, 1179–1180.

Kechavarzi, B., and Janga, S.C. (2014). Dissecting the expression landscape of RNA-binding proteins in human cancers. Genome Biol. *15*, R14.

Kryndushkin, D.S., Alexandrov, I.M., Ter-Avanesyan, M.D., and Kushnirov, V.V. (2003). Yeast [PSI+] prion aggregates are formed by small Sup35 polymers fragmented by Hsp104. J. Biol. Chem. *278*, 49636–49643.

Kuznetsova, I.M., Turoverov, K.K., and Uversky, V.N. (2014). What macromolecular crowding can do to a protein. Int. J. Mol. Sci. *15*, 23090–23140.

Larson, A.G., Elnatan, D., Keenen, M.M., Trnka, M.J., Johnston, J.B., Burlingame, A.L., Agard, D.A., Redding, S., and Narlikar, G.J. (2017). Liquid droplet formation by HP1α suggests a role for phase separation in heterochromatin. Nature *547*, 236–240.

Li, L., and Kowal, A.S. (2012). Environmental regulation of prions in yeast. PLoS Pathog. *8*, e1002973.

Li, P., Banjade, S., Cheng, H.C., Kim, S., Chen, B., Guo, L., Llaguno, M., Hollingsworth, J.V., King, D.S., Banani, S.F., et al. (2012). Phase transitions in the assembly of multivalent signalling proteins. Nature *483*, 336–340.

Liebman, S.W., and Chernoff, Y.O. (2012). Prions in yeast. Genetics *191*, 1041–1072.

Lin, Y., Protter, D.S., Rosen, M.K., and Parker, R. (2015). Formation and Maturation of Phase-Separated Liquid Droplets by RNA-Binding Proteins. Mol. Cell *60*, 208–219.

Love, M.I., Huber, W., and Anders, S. (2014). Moderated estimation of fold change and dispersion for RNA-seq data with DESeq2. Genome Biol. *15*, 550.

March, Z.M., King, O.D., and Shorter, J. (2016). Prion-like domains as epigenetic regulators, scaffolds for subcellular organization, and drivers of neurodegenerative disease. Brain Res. *1647*, 9–18.

McKinley, M.P., Bolton, D.C., and Prusiner, S.B. (1983). A protease-resistant protein is a structural component of the scrapie prion. Cell *35*, 57–62.

Molliex, A., Temirov, J., Lee, J., Coughlin, M., Kanagaraj, A.P., Kim, H.J., Mittag, T., and Taylor, J.P. (2015). Phase separation by low complexity domains promotes stress granule assembly and drives pathological fibrillization. Cell *163*, 123–133.

Nakayashiki, T., Kurtzman, C.P., Edskes, H.K., and Wickner, R.B. (2005). Yeast prions [URE3] and [PSI+] are diseases. Proc. Natl. Acad. Sci. USA *102*, 10575–10580.

Nishtala, S., Neelamraju, Y., and Janga, S.C. (2016). Dissecting the expression relationships between RNA-binding proteins and their cognate targets in eukaryotic post-transcriptional regulatory networks. Sci. Rep. *6*, 25711.

Niu, N., Xiang, J.F., Yang, Q., Wang, L., Wei, Z., Chen, L.L., Yang, L., and Zou, W. (2017). RNA-binding protein SAMD4 regulates skeleton development through translational inhibition of Mig6 expression. Cell Discov. *3*, 16050.

Oberstrass, F.C., Lee, A., Stefl, R., Janis, M., Chanfreau, G., and Allain, F.H.T. (2006). Shape-specific recognition in the structure of the Vts1p SAM domain with RNA. Nat. Struct. Mol. Biol. *13*, 160–167.

Patel, A., Lee, H.O., Jawerth, L., Maharana, S., Jahnel, M., Hein, M.Y., Stoynov, S., Mahamid, J., Saha, S., Franzmann, T.M., et al. (2015). A Liquid-to-Solid Phase Transition of the ALS Protein FUS Accelerated by Disease Mutation. Cell *162*, 1066–1077.

Patino, M.M., Liu, J.J., Glover, J.R., and Lindquist, S. (1996). Support for the prion hypothesis for inheritance of a phenotypic trait in yeast. Science *273*, 622–626.

Paushkin, S.V., Kushnirov, V.V., Smirnov, V.N., and Ter-Avanesyan, M.D. (1997). In vitro propagation of the prion-like state of yeast Sup35 protein. Science *277*, 381–383.

Peng, K., Radivojac, P., Vucetic, S., Dunker, A.K., and Obradovic, Z. (2006). Length-dependent prediction of protein intrinsic disorder. BMC Bioinformatics *7*, 208.

Protter, D.S.W., Rao, B.S., Van Treeck, B., Lin, Y., Mizoue, L., Rosen, M.K., and Parker, R. (2018). Intrinsically Disordered Regions Can Contribute Promiscuous Interactions to RNP Granule Assembly. Cell Rep. *22*, 1401–1412.

Prusiner, S.B. (1982). Novel proteinaceous infectious particles cause scrapie. Science *216*, 136–144.

Prusiner, S.B. (1984). Prions: novel infectious pathogens. Adv. Virus Res. *29*, 1–56.

Prusiner, S.B. (1997). Prion diseases and the BSE crisis. Science *278*, 245–251.

Prusiner, S.B., McKinley, M.P., Bowman, K.A., Bolton, D.C., Bendheim, P.E., Groth, D.F., and Glenner, G.G. (1983). Scrapie prions aggregate to form amyloid-like birefringent rods. Cell *35*, 349–358.

Ray, D., Kazan, H., Cook, K.B., Weirauch, M.T., Najafabadi, H.S., Li, X., Gueroussov, S., Albu, M., Zheng, H., Yang, A., et al. (2013). A compendium of RNA-binding motifs for decoding gene regulation. Nature *499*, 172–177.

Rendl, L.M., Bieman, M.A., and Smibert, C.A. (2008). *S. cerevisiae* Vts1p induces deadenylation-dependent transcript degradation and interacts with the Ccr4p-Pop2p-Not deadenylase complex. RNA *14*, 1328–1336.

Riback, J.A., Katanski, C.D., Kear-Scott, J.L., Pilipenko, E.V., Rojek, A.E., Sosnick, T.R., and Drummond, D.A. (2017). Stress-Triggered Phase Separation Is an Adaptive, Evolutionarily Tuned Response. Cell *168*, 1028–1040.e1019.

Rosenzweig, R., Nillegoda, N.B., Mayer, M.P., and Bukau, B. (2019). The Hsp70 chaperone network. Nat. Rev. Mol. Cell Biol. *20*, 665–680.

Saad, S., Cereghetti, G., Feng, Y., Picotti, P., Peter, M., and Dechant, R. (2017). Reversible protein aggregation is a protective mechanism to ensure cell cycle restart after stress. Nat. Cell Biol. *19*, 1202–1213.

Sabari, B.R., Dall'Agnese, A., Boija, A., Klein, I.A., Coffey, E.L., Shrinivas, K., Abraham, B.J., Hannett, N.M., Zamudio, A.V., Manteiga, J.C., et al. (2018). Coactivator condensation at super-enhancers links phase separation and gene control. Science *361*, eaar3958.

Schneider, C.A., Rasband, W.S., and Eliceiri, K.W. (2012). NIH Image to ImageJ: 25 years of image analysis. Nat. Methods *9*, 671–675.

She, R., Chakravarty, A.K., Layton, C.J., Chircus, L.M., Andreasson, J.O.L., Damaraju, N., McMahon, P.L., Buenrostro, J.D., Jarosz, D.F., and Greenleaf, W.J. (2017). Comprehensive and quantitative mapping of RNA-protein interactions across a transcribed eukaryotic genome. Proc. Natl. Acad. Sci. USA *114*, 3619–3624.

Shin, Y., and Brangwynne, C.P. (2017). Liquid phase condensation in cell physiology and disease. Science *357*, eaaf4382.

Shorter, J. (2008). Hsp104: a weapon to combat diverse neurodegenerative disorders. Neurosignals *16*, 63–74.

Shorter, J., and Lindquist, S. (2004). Hsp104 catalyzes formation and elimination of self-replicating Sup35 prion conformers. Science *304*, 1793–1797.

Smibert, C.A., Wilson, J.E., Kerr, K., and Macdonald, P.M. (1996). smaug protein represses translation of unlocalized nanos mRNA in the Drosophila embryo. Genes Dev. *10*, 2600–2609.

Smith, J., Calidas, D., Schmidt, H., Lu, T., Rasoloson, D., and Seydoux, G. (2016). Spatial patterning of P granules by RNA-induced phase separation of the intrinsically-disordered protein MEG-3. eLife *5*, e21337.

Song, Y., Wu, Y.X., Jung, G., Tutar, Y., Eisenberg, E., Greene, L.E., and Masison, D.C. (2005). Role for Hsp70 chaperone in Saccharomyces cerevisiae prion seed replication. Eukaryot. Cell *4*, 289–297.

Stefl, R., Skrisovska, L., and Allain, F.H. (2005). RNA sequence- and shape-dependent recognition by proteins in the ribonucleoprotein particle. EMBO Rep. *6*, 33–38.

Strom, A.R., Emelyanov, A.V., Mir, M., Fyodorov, D.V., Darzacq, X., and Karpen, G.H. (2017). Phase separation drives heterochromatin domain formation. Nature *547*, 241–245.

Suzuki, G., Shimazu, N., and Tanaka, M. (2012). A yeast prion, Mod5, promotes acquired drug resistance and cell survival under environmental stress. Science *336*, 355–359.

Szklarczyk, D., Franceschini, A., Wyder, S., Forslund, K., Heller, D., Huerta-Cepas, J., Simonovic, M., Roth, A., Santos, A., Tsafou, K.P., et al. (2015). STRING v10: protein-protein interaction networks, integrated over the tree of life. Nucleic Acids Res. *43*, D447–D452.

Tadros, W., Goldman, A.L., Babak, T., Menzies, F., Vardy, L., Orr-Weaver, T., Hughes, T.R., Westwood, J.T., Smibert, C.A., and Lipshitz, H.D. (2007). SMAUG is a major regulator of maternal mRNA destabilization in Drosophila and its translation is activated by the PAN GU kinase. Dev. Cell *12*, 143–155.

Tanaka, M., Chien, P., Naber, N., Cooke, R., and Weissman, J.S. (2004). Conformational variations in an infectious protein determine prion strain differences. Nature *428*, 323–328.

Tapia, H., and Koshland, D.E. (2014). Trehalose is a versatile and long-lived chaperone for desiccation tolerance. Curr. Biol. *24*, 2758–2766.

Teste, M.A., Duquenne, M., François, J.M., and Parrou, J.L. (2009). Validation of reference genes for quantitative expression analysis by real-time RT-PCR in Saccharomyces cerevisiae. BMC Mol. Biol. *10*, 99.

Thévenaz, P., Ruttimann, U.E., and Unser, M. (1998). A pyramid approach to subpixel registration based on intensity. IEEE Trans. Image Process. *7*, 27–41.

Thompson, J.R., Register, E., Curotto, J., Kurtz, M., and Kelly, R. (1998). An improved protocol for the preparation of yeast cells for transformation by electroporation. Yeast *14*, 565–571.

Tokuriki, N., Kinjo, M., Negi, S., Hoshino, M., Goto, Y., Urabe, I., and Yomo, T. (2004). Protein folding by the effects of macromolecular crowding. Protein Sci. *13*, 125–133.

Toombs, J.A., McCarty, B.R., and Ross, E.D. (2010). Compositional determinants of prion formation in yeast. Mol. Cell. Biol. *30*, 319–332.

Toyama, B.H., Kelly, M.J., Gross, J.D., and Weissman, J.S. (2007). The structural basis of yeast prion strain variants. Nature *449*, 233–237.

Uptain, S.M., and Lindquist, S. (2002). Prions as protein-based genetic elements. Annu. Rev. Microbiol. *56*, 703–741.

Uversky, V.N. (2014). Introduction to intrinsically disordered proteins (IDPs). Chem. Rev. *114*, 6557–6560.

Uversky, V.N. (2017). Intrinsically disordered proteins in overcrowded milieu: Membrane-less organelles, phase separation, and intrinsic disorder. Curr. Opin. Struct. Biol. *44*, 18–30.

van den Berg, B., Wain, R., Dobson, C.M., and Ellis, R.J. (2000). Macromolecular crowding perturbs protein refolding kinetics: implications for folding inside the cell. EMBO J. *19*, 3870–3875.

van der Lee, R., Buljan, M., Lang, B., Weatheritt, R.J., Daughdrill, G.W., Dunker, A.K., Fuxreiter, M., Gough, J., Gsponer, J., Jones, D.T., et al. (2014). Classification of intrinsically disordered regions and proteins. Chem. Rev. *114*, 6589–6631.

Wickner, R.B. (1994). [URE3] as an altered URE2 protein: evidence for a prion analog in Saccharomyces cerevisiae. Science *264*, 566–569.

Wickner, R.B., Edskes, H.K., Ross, E.D., Pierce, M.M., Baxa, U., Brachmann, A., and Shewmaker, F. (2004). Prion genetics: new rules for a new kind of gene. Annu. Rev. Genet. *38*, 681–707.

Wickner, R.B., Edskes, H.K., and Shewmaker, F. (2006). How to find a prion: [URE3], [PSI+] and [beta]. Methods *39*, 3–8.

Wilson, B.A., Petrov, D.A., and Messer, P.W. (2014). Soft selective sweeps in complex demographic scenarios. Genetics *198*, 669–684.

Winston, F., Dollard, C., and Ricupero-Hovasse, S.L. (1995). Construction of a set of convenient Saccharomyces cerevisiae strains that are isogenic to S288C. Yeast *11*, 53–55.

Woodruff, J.B., Ferreira Gomes, B., Widlund, P.O., Mahamid, J., Honigmann, A., and Hyman, A.A. (2017). The Centrosome Is a Selective Condensate that Nucleates Microtubules by Concentrating Tubulin. Cell *169*, 1066–1077.e1010.

Zhu, L., and Brangwynne, C.P. (2015). Nuclear bodies: the emerging biophysics of nucleoplasmic phases. Curr. Opin. Cell Biol. *34*, 23–30.

STAR★METHODS

KEY RESOURCES TABLE

REAGENT or RESOURCE	SOURCE	IDENTIFIER
Critical Commercial Assays		
KAPA SYBR Fast qPCR	Kapa Biosystems	Cat# KK4601
Bio-Rad Protein Assay	BioRad	Cat# 500-0006
TURBO DNA-free™ Kit	Invitrogen	AM1907
Nucleic acid based reagents		
Oligo dT-20 primer	Invitrogen	Cat#18418-020
Salmon sperm DNA	Sigma	Cat# D1626-5G
Primers used	This study	https://benchling.com/s/etr-1TQzTbjJbsbzF7q9ziGY/edit
Synthetic RNAs used	*This study*	https://benchling.com/s/etr-Rkw1WTrjbMQ4L9obRqwS/edit
Experimental Models: Organisms/Strains		
BY4741 mat a	(Winston et al., 1995)	N/A
BY4741 *vts1Δ*	(Giaever et al., 2002)	N/A
BY4741 - [*SMAUG*$^{+}$]	(Chakrabortee et al., 2016)	N/A
Cured [*SMAUG*$^{+}$]	This paper	See STAR Methods for details
BY4741 – *ynr034w-a::URA3*	This paper	See STAR Methods for details
BY4741 [*SMAUG*$^{+}$] – *ynr034w-a::URA3*	This paper	See STAR Methods for details
BY4741 *vts1Δ* – *ynr034w-a::URA3*	This paper	See STAR Methods for details
BY4741 – Neon tagged HO locus	This paper	See STAR Methods for details
BY4741 – mKate tagged HO locus	This paper	See STAR Methods for details
BY4741 - [*SMAUG*$^{+}$] – Neon tagged HO locus	This paper	See STAR Methods for details
BY4741 - [*SMAUG*$^{+}$] – mKate tagged HO locus	This paper	See STAR Methods for details
BY4741 *ccr4Δ*	Original paper	See STAR Methods for details
BY4742 CCR4-GFP	Schuldiner group SWAT	See STAR Methods for details
BY4742 POP2-GFP	Schuldiner group SWAT	See STAR Methods for details
Recombinant DNA		
pDEST17-His10-Smt3-ccdB-SNAP	This paper	https://benchling.com/s/seq-LMKTgagCMmODB7Z1kwPZ/edit
pDEST17-His10-Smt3-FL-Vts1-SNAP	This paper	https://benchling.com/s/seq-CLjAQgc8riqrbYUvliMi/edit
pDEST17-His10-Smt3-RBD-Vts1-SNAP	This paper	https://benchling.com/s/seq-XzYoygzsun9aVTBReOL6/edit
pDEST17-His10-Smt3-IDR-Vts1-SNAP	This paper	https://benchling.com/s/seq-X0Zje0lRMP80NkuroL30/edit
pDEST17-His10-Smt3-ccdB	This paper	https://benchling.com/s/seq-NNZpPlJzBZuse2veAuh7/edit
pDEST17-His10-Smt3-FL-Vts1	This paper	https://benchling.com/s/seq-NNZpPlJzBZuse2veAuh7/edit
pGFP-SRE+ reporter	A gift from C. Smibert (U of Toronto)	https://benchling.com/s/seq-yGrofWzbQtqAAMdRVX8Q/edit
pGFP-SRE- reporter	A gift from C. Smibert (U of Toronto)	https://benchling.com/s/seq-X3Z4SsQEbmOfpw6qBbns/edit
pAG416GPD-SSA1(K69M)	(Jarosz et al., 2014)	N/A
pFL-hSmaug1-SNAP	This paper	https://benchling.com/s/seq-ylumYnnWbvbQAstnTqM7/edit

(*Continued on next page*)

Continued

REAGENT or RESOURCE	SOURCE	IDENTIFIER
pDONR221_hSmaug1	This paper	https://benchling.com/s/seq-OGdGOQpIjlDQp1rWv1FZ/edit
pAG426_GAL-hSmaug1-eGFP	This paper	https://benchling.com/s/seq-iPbdWuaQapXoYPhicm41/edit
pSchan(Ura3)	A gift from R. Halfmann (Stowers Institute)	https://benchling.com/s/seq-l97S6T8qFH1Nal77tgwh/edit
pSK275_TDH3_Neon	A gift from B. Wong (Khalil lab, BU)	https://benchling.com/s/seq-ZaCbBK9aOLKqR6Lcai81/edit
pSK275_TDH3_mKate2	A gift from Brandon Wong (Khalil lab, BU)	https://benchling.com/s/seq-sC9Tx4CfcTHSuUduplxT/edit
Advanced Gateway Destination Vectors	(Alberti et al., 2007)	http://www.addgene.org/kits/lindquist-yeast-gateway/
Chemicals, recombinant proteins and miscellaneous resources		
SNAP-Surface® 549	New England Biolabs	Cat# S9112S
SNAP-Surface® 488	New England Biolabs	Cat# S9124S
Poly ethylene glycol (PEG) – MW 8000	Millipore Sigma	Cat# 6510-OP
cOmplete™ Protease Inhibitor Cocktail	Roche	Cat# 11836145001
Sodium Dodecyl Sulfate	Sigma Aldrich	Cat# L3771-500G
Thioflavin T	Sigma Aldrich	Cat# T3516-5G
Amino acid supplements (CSM formulations)	Sunrise Science Products	https://sunrisescience.com/products/growth-media/amino-acid-supplement-mixtures/csm-formulations/
Bovine Serum Albumin	Thermo Fisher Scientific	Cat# 23209
Proteinase K	Fisher Scientific	Cat# BP1700-500
NM-Sup35 fibrils	Gift from Dr. Kendra K. Frederick	(Frederick et al., 2015)
Superscript Reverse Transcriptase	Invitrogen	Cat# 18064014
RNaseOUT	Invitrogen	Cat# 10777019
Anti-GFP antibody (JL-8)	Takara	Cat# 632380; RRID:AB_10013427
Zymolyase®-100T	Sunrise Science Products	Cat# 0766555
Ni-NTA Agarose beads	QIAGEN	Cat# 30250
SP-Sepharose beads	GE Healthcare	Cat# 17-0729-01
Superdex S200 Increase column	GE Healthcare	Cat# 28990944
Agarose	Goldbio	Cat# A-201-500
SDS-PAGE gels	Genscript	Cat# M41215
Native TBE gels	Invitrogen	Cat# EC6225BOX
Slide-A-Lyzer dialysis cassettes	Thermo Fisher Scientific	https://www.thermofisher.com/us/en/home/life-science/protein-biology/protein-purification-isolation/protein-dialysis-desalting-concentration/dialysis-products/slide-a-lyzer-dialysis-cassettes.html
Formvar/Carbon copper grids	Electron Microscopy Sciences	Cat# FCF300-Cu
Electroporation cuvettes	BioRad	Cat# 1652086
Epifluorescence microscope	Leica	DMI6000
Cryo Mill	Retsch	20.749.0001
Eon™ microplate spectrophotometer	BioTek	N/A
Software and Algorithms		
RStudio	RStudio Inc.	Version 0.99.903
DeSeq2	(Love et al., 2014)	https://bioconductor.org/packages/release/bioc/html/DESeq2.html
kallisto	(Bray et al., 2016)	https://pachterlab.github.io/kallisto/
ImageJ	NIH	https://imagej.nih.gov/ij/

(*Continued on next page*)

Continued

REAGENT or RESOURCE	SOURCE	IDENTIFIER
Image Lab	BioRad	Version 5.2.1
Prism	GraphPad Software Inc.	Version 7.0d
Cell Profiler	(Kamentsky et al., 2011)	CellProfiler 3.1.5
FlowJo	FlowJo, LLC	FlowJo 10.2
Leica LAS X Core Image Analysis Software	Leica, Inc.	https://www.leica-microsystems.com/products/microscope-software/
Gen5	BioTek	Version 2.09
Unicorn™	GE Healthcare	Version 7.0
DISOPRED	(Jones and Cozzetto, 2015)	http://bioinf.cs.ucl.ac.uk/psipred/?disopred=1
STRING	(Szklarczyk et al., 2015)	https://string-db.org/
Deposited Data		
Gene Expression Omnibus (GEO)	This paper	GEO: GSE138557
Mendeley Data	This paper	10.17632/gzc6z9dkhy.1

LEAD CONTACT AND MATERIALS AVAILABILITY

Correspondence and requests for materials should be addressed to Lead Contact Daniel F. Jarosz (danjarosz.aa@gmail.com). All unique reagents generated in this study are available from the Lead Contact without restriction.

EXPERIMENTAL MODEL AND SUBJECT DETAILS

S. cerevisiae strains were obtained from the sources indicated (Key Resources Table). All *S. cerevisiae* strains were stored as glycerol stocks at −80C. Before use, strains were either revived on YPD or on synthetically defined medium (*as necessary*). Antibiotics or synthetically defined medium with key nutrients removed were used as indicated to maintain plasmid selection. Growth was at 30°C unless otherwise mentioned. Typically, for plasmid transformations, a standard lithium–acetate protocol was used (Gietz et al., 1992). First, cells were inoculated and grown to saturation in rich media (YPD - 10 g/l yeast extract, 20 g/l dextrose, 20 g/l peptone, sterilized by autoclaving). The cells were then diluted and regrown to mid-exponential phase (OD_{600} ~0.6 - 0.8), pelleted, washed in sterile water, and resuspended in a transformation master mix (240 μL of PEG 3500 50% (w/v), 36 μL 1 M Lithium acetate, 50 μL denatured salmon sperm carrier DNA (2 mg/ml), 34 μL plasmid DNA (0.1-1 μg total plasmid), and sterile water to a final volume of 360 μL). Cells were incubated in the transformation master mix at 42°C for 30 min. Following incubation, cells were harvested, resuspended in 1 mL sterile water, and ~10-100 μL was plated on selective medium.

Standard electroporation protocols were used for transformations to integrate recombinant DNA into genomic loci of *S. cerevisiae* (Thompson et al., 1998). All reagents used were sterilized by autoclaving or filter sterilizing through a pre-sterile 0.22 μm filter. Individual colonies of requisite strains were inoculated into YPD liquid medium (5 ml) and grown to saturation overnight at 30°C. Cultures were then diluted to an OD600 of 0.1 in a 50 mL volume and then grown for a ~3-4 hours to mid-exponential phase (OD600 ~0.6 – 0.8). Cells were washed once in sterile water and resuspended in TE buffer (18 ml, 10 mM Tris-HCl ph 7.5, 1 mM EDTA, 0.22 μm filter sterilized). Next, we added 1 M Lithium acetate (2 ml) and incubated the cells on a roller drum at 30°C for 45 min, followed by addition of1 M DTT (500 μl). We then incubated cells for 15 min at 30°C, harvested them (1000 × g, 5 min), and then washed them with sterile water followed by 1 M sorbitol. Finally, we resuspended the washed cells in 120 μl of pre-chilled 1 M sorbitol. For transformation, we added 1.7 μl carrier salmon sperm DNA (2 mg/ml) and ~1 μg of desired recombinant DNA cassette to 40 μl of cells and transferred this mixture to a pre-chilled electroporation cuvette. Electroporation was performed at 1.5 kV, 25 μF and 200 Ω. A pre-chilled mixture of YPD with1 M sorbitol (1 ml) was immediately added to the electroporated cells and the cells were recovered overnight and subsequently plated on selective medium plates. Individual inductants of [*SMAUG*$^+$] were generated previously (Chakrabortee et al., 2016). To eliminate [*SMAUG*$^+$] from cells, we used a transient expression of dominant negative mutant of Hsp70 (*SSA1*^{K69M}) as we have demonstrated previously (Chakrabortee et al., 2016). [*SMAUG*$^+$] cells were transformed with plasmids expressing *SSA1*^{K69M} from a strong constitutive promoter (GPD) and with *URA3* selection marker (see Key Resources Table). Transformants were passaged twice on selective medium, followed by two passages on plates containing 5-fluoroorotic acid (5-FOA) to allow plasmid loss, which was confirmed by the absence of growth on selective medium (SD-URA). This strain was then passaged on YP-Glycerol plates to ensure that these cells were respiration-competent and then twice more on YPD before being used in our assays.

For cytoduction experiments, we used naive and [*SMAUG*$^+$] strains (BY4742 genetic background) with a defective KAR allele (*kar1-15*) (Chakrabortee et al. 2016), as donors for cytoplasmic transfer (see Figure S4D for *schematic*). This defective KAR allele prevents nuclear fusion during mating while permitting cytoplasmic transfer. Recipient strains harboring gene deletions (*ccr4Δ*) of

opposite mating type harboring auxotrophic markers distinct from those in the naive and [*SMAUG*$^+$] donor strains. The recipient strains were also converted to respiration-incompetent ('petite') strains with growth on ethidium bromide (Chakrabortee et al. 2016). This allowed cytoplasmic transfer from donor strains to be scored through the restoration of mitochondrial respiration, while selecting for auxotrophic markers unique to the recipient strain. The recipient and donor strains were mixed together on YPD-agar, followed by selection of heterokaryons on dropout media containing glycerol as a carbon source. This selection step was designed to select buds that were respiration competent (i.e., had cytoplasmic transfer from the donor strains) and had the genetic markers of the recipient strain. Additionally, we confirmed that the selected cytoductants were not diploids by replica plating them on to plates selecting for diploid specific genetic markers and confirming their lack of growth on such a plate.

METHOD DETAILS

Disorder Analyses

The polypeptide sequence of Vts1 orthologs across the fungal clade were obtained from the yeast gene order browser (Byrne and Wolfe, 2005). The disorder score of individual amino acids across polypeptides was measured *in silico* using Disopred or VSL2 server (Jones and Cozzetto, 2015; Peng et al., 2006). The conservation of disorder score at any individual region of the protein was done by constructing a metaprotein of normalized length using custom R script. A heatmap was generated from this conservation score.

Protein expression and purification

A gateway compatible plasmid was designed for protein expression such that any open reading frame of choice could be N-terminally linked to a His^{10}-Smt3 tag and C-terminally to a SNAP tag (see Key Resources Table). Full-length Vts1 (Vts1), isolated disordered domain (IDR-Vts1) and isolated RNA binding domain (RBD-Vts1) were cloned into this expression plasmid and subsequently transformed into *E. coli* BL21(DE3) cells. A 4-l culture expressing Vts1 (3 L for IDR-Vts1, 1 L for RBD-Vts1) was derived from a single transformant grown at 37°C in Luria-Bertani medium containing 100 μg/ml ampicillin until the OD_{600} reached ~0.8. The culture was then adjusted to 1 mM IPTG and incubated for 3 h at 37°C with continuous shaking. Cells were harvested by centrifugation, and the pellet was stored at −80°C. All subsequent procedures were performed at 4°C. Thawed cell pellets were resuspended in 100 mL of buffer A (50 mM Tris-HCl, pH 7.4, 250 mM NaCl, 10% sucrose). Lysozyme was added to a final concentration of 0.2 mg/ml. After mixing for 1 h, the lysate was sonicated to reduce viscosity and insoluble material was removed by centrifugation for 30 min at 30,000 × g. The soluble extract was mixed for 1 h with 10 mL of a 50% slurry of Ni-NTA resin (QIAGEN) that had been equilibrated in buffer A. The resin was recovered by centrifugation and resuspended in 20 mL of buffer B (50 mM Tris-HCl, pH 7.4, 150 mM NaCl, 10% glycerol) containing 25 mM imidazole. The cycle of centrifugation and resuspension of the resin was repeated thrice, after which the resin (5 ml) was poured into a column. The column was washed serially with 10 mL of buffer C (50 mM Tris-HCl, pH 7.4, 2 M KCl) and 10 mL of buffer B containing 50 mM imidazole. The bound proteins were eluted stepwise in 10 mL aliquots of 100, 200, 300, and 400 mM imidazole in buffer B. The elution profile was monitored by SDS-PAGE. The 200, 300, and 400 mM imidazole eluate fractions containing protein of interest (His^{10}-Smt3-Vts1-SNAP) were pooled and supplemented with Smt3- specific protease Ulp1 (to attain a Ulp1:His^{10}Smt3-Vts1-SNAP ratio of 1:100). Smt3-specific protease Ulp1 was a kind gift from Christopher D. Lima. The mixture was dialyzed overnight (~16h) against 2 l of buffer B supplemented with 25 mM imidazole and 2 mM DTT using a Slide-A-Lyzer dialysis cassette (10K MWCO).

The dialysate was then mixed for 1.5 h with 6 mL of a 50% slurry of Ni-NTA resin that had been equilibrated in buffer B containing 25 mM imidazole and 2 mM DTT. The resin (3 ml) was poured into a column, washed with 50 mM and 100 mM imidazole in buffer B, and then eluted with 500 mM imidazole in buffer B. The Vts1-SNAP protein was recovered in the flow-through and the wash fractions (containing 50 and 100 mM imidazole) and the His^{10}Smt3 tag was recovered in the 500 mM imidazole fraction. The flowthrough and wash fractions were pooled after initial analyses by SDS-PAGE and then dialyzed for 3 h against buffer D (50 mM Tris-HCl pH 8.0, 20 mM NaCl, 2 mM DTT, 10% glycerol). The dialysate was then mixed for 1.5 h with 2 mL of a 50% slurry of SP-Sepharose resin (GE) that had been equilibrated in buffer D. The resin (1 ml) was then poured into a column and eluted stepwise with buffer D containing 50 mM, 100 mM, 150 mM, 200 mM, 250 mM, and 500 mM NaCl. Vts1-SNAP was recovered in the 150 mM – 250 mM NaCl window. This pooled fraction was concentrated by centrifugal ultrafiltration and gel-filtered through a 24 mL Superdex 200 Increase column (GE Healthcare) equilibrated in buffer E (50 mM Tris-HCl, pH 8.0, 150 mM NaCl, 2 mM DTT, 10% glycerol), at a flow rate of 0.3 ml/min. The peak Vts1-SNAP fractions were pooled and concentrated by centrifugal ultrafiltration to ~0.8 mg/ml. The yield of the Vts1-SNAP was around 1.5 mg. RBD-Vts1 was prepped in an identical manner starting from the appropriate expression construct. Non-SNAP tagged Vts1 protein was prepped using an analogous expression vector that lacked the C-terminal SNAP tag. Key steps used during protein purification have been summarized in Figure S2B.

Sizing analyses

A 24 mL Superdex 200 Increase column (GE Healthcare) was equilibrated in the following buffer (50 mM Tris-HCl, pH 8.0, 150 mM NaCl, 2 mM DTT, 10% glycerol), at a flow rate of 0.3 ml/min. Standards from the GE HMW Calibration Kit were dissolved in this buffer to a final concentration of 2 mg/ml each - Thyroglobulin (660 kDa); Ferritin (440 kDa); Aldolase (158 kDa), Conalbumin (75 kDa), Ovalbumin (43 kDa) and separated on the size-exclusion column and further analyzed by SDS-PAGE and Coomassie staining. Blue Dextran (avg MW ~2000 kDa) was used to mark the void volume of the column. The partition coefficients were plotted against

MW to obtain a calibration curve (Figure S2D). Vts1-SNAP variants (full-length, IDR and RBD) were analyzed under identical buffer and flow conditions on the Superdex 200 Increase gel filtration column and their molecular weights was determined from this calibration curve.

Electrophoretic mobility shift assay (EMSA)

Varying amounts of Vts1-SNAP protein as indicated (Figure 2D) were incubated for 30 minutes at 4°C with a single hairpin Smaug recognition element (SRE-C) that is a previously known strong binder of Vts1 (She et al., 2017). This binding reaction was carried out in the following buffer conditions – 20 mM Tris-HCl pH 7.4, 150 mM NaCl, 0.01% Tween 20, 5 mM $MgCl_2$. Following incubation these reaction mixtures were analyzed on an 8% Tris-borate-EDTA (TBE) gels run under following buffer conditions (45 mM Tris-borate, 1mM EDTA) for 1h at 4°C. The gels were imaged using a BioRad ChemiDoc with appropriate filter sets for imaging fluorescein.

Labeling of purified protein

Purified Vts1 was labeled with *in vitro* SNAP-surface™ dyes (NEB) in the following buffer conditions – 50 mM Tris-HCl pH7.4, 100 mM NaCl, 0.1% Tween 20 and 2mM DTT. Typically, a 2:1 molar ratio of dye to protein was used for the labeling reactions and reaction volume was maintained at 80 μl (She et al., 2017). The labeling reaction was carried out at 4°C overnight. Following labeling, the excess dye was cleaned up using Zeba spin desalting columns (7K MWCO, Thermo Scientific) using manufacturer's instructions. Finally, the labeled protein was resuspended in buffer TMK (100 mM Tris•HCl, pH 7.4, 80 mM KCl, 10 mM $MgCl_2$, 1 mM DTT).

Blotting for protein levels in naive and [SMAUG$^+$] cells

Overnight cultures (5 ml) of yeast strains as specified were grown and cells were pelleted by centrifugation for 5 min at 3000 × g. Cell pellets were washed with sterile water and resuspended in 100 μl of 20% (v/v) tri-chloro acetic acid (TCA) solution supplemented with protease inhibitors. The samples were further lysed by bead beating and pelleted by centrifuging for 10 min at 3000 × g. Pellets from these samples were re-suspended in Laemmli buffer, a small fraction of these samples were run on SDS-PAGE gel, transferred to a PVDF membrane and probed with anti-GFP antibody (as stated in the Key Resources Table).

In vitro assembly

Purified Vts1 was typically assembled into condensates under the following buffer conditions (25 mM Tris-HCl pH 7.4, 75 mM KCl, 1.25% glycerol, 0.5 mM DTT) with amounts (v/v) of PEG 8K as mentioned in the respective figure panels. Formation of Vts1 condensates were observed at a final concentration of 5% (v/v) of PEG 8K and within 1 h at room temperature. Robust condensation was observed upto a 2.5% final concentration of PEG 8K. Unless otherwise mentioned, Vts1 condensates were formed at 5% final PEG 8K and after 1 h at room temperature. For *in vitro* seeding by pre-assembled Vts1, pre-assembled Vts1-$SNAP^{549}$ was incubated with unassembled Vts1-$SNAP^{488}$ (molar ratio of ~1:10 of Vts1-$SNAP^{549}$: Vts1-$SNAP^{488}$) for nearly 48 h at room temperature under the following buffer conditions (25 mM Tris-HCl pH 7.4, 75 mM KCl, 1% glycerol, 0.5 mM DTT, 1% (v/v) PEG 8K). Buffer matched controls lacked pre-assembled Vts1-SNAP549 but had 1.4% PEG 8K to ensure commensurate crowder concentration. The intensity for all colocalization events in pre-assembled Vts1 sample was calculated. For unassembled sample, intensity of masks of identical area was calculated. For lysate based seeding experiments, yeast cell lysates were prepared from 100 mL cell culture of appropriate yeast strain at mid exponential phase using cryo-milling methods (*see below*) and were incubated with labeled Vts1-$SNAP^{549}$ (molar ratio of Vts1 from lysate: Vts1-$SNAP^{549}$ was ~1:163) at room temperature for 1-2 weeks in buffer TMK (100 mM Tris•HCl, pH 7.4, 80 mM KCl, 10 mM $MgCl_2$, 1 mM DTT) lacking any crowder. Relative abundances of proteins were used from systems-wide measurements in budding yeast (Ghaemmaghami et al., 2003).

Condensate assays

• *Microscopy of condensates*

Microscopy was performed using a Leica inverted fluorescence microscope (Leica DMI6000) with a Hammamatsu Orca 4.0 camera. Vts1 condensates were imaged after short (30 min –1 h) or long (overnight or longer) incubations as stated. Exposure times in the DIC channel were typically 20 - 50 ms and in the fluorescence channel around 5 - 16 ms. Across a single experiment, exposure times were maintained to be the same in all samples. The filter blocks used for labeling the differently labeled moieties are as follows: $SNAP^{549}$ labeled condensates – CY3, $SNAP^{488}$ labeled condensates and fluorescein labeled RNAs– GFP. All images were contrast adjusted to identical levels and the area of condensates was quantified across replicates using ImageJ.

• *NAGE of condensates*

Given the size and detergent susceptibility of Vts1 condensates, we reasoned that we would be able to separate the condensates from their unassembled protein using an ideological counterpart to SDD-AGE in which the detergent had been left out. So using native agarose gel electrophoresis (NAGE), we were able to observe that the fluorescently-labeled assembled Vts1 migrated very near to the well whereas unassembled Vts1 would migrate far into the gel. The RBD-Vts1 treated identically did not form a similarly retarded species on the gel. A critical control where the addition of the crowding agent was done immediately prior to running the gel did not form the species retained in the well indicating that the crowding buffer alone did not lead to aberrant patterns in gel migration. In brief, $SNAP^{549}$ labeled Vts1 condensates were loaded onto a 0.5% Agarose gel that was run under the following buffer conditions (25 mM Tris pH 8.5 and 250 mM glycine) overnight at 4°C under a constant voltage of 35 V. The samples were loaded onto the

agarose gel using the following loading buffer composition (12.5 mM Tris-HCl pH 7.4, 2% glycerol (v/v), 0.02% bromophenol blue and 1% Triton). The gels were imaged using a BioRad Chemidoc with Alexa546 filter cubes.

- ***Detergent reactivity***

Labeled Vts1 condensates that have been formed from overnight assembly reactions were exposed to increasing amounts of sodium dodecyl sulfate (SDS) or cetyl trimethyl ammonium bromide (CTAB; as stated) from a 10% (w/v) stock solution. These assemblies were incubated with detergent at room temperature for 30 minutes and then imaged using a fluorescence microscope or analyzed by native agarose gel electrophoresis.

- **In vitro *reversibility***

A 50 μl reaction comprising labeled Vts1 condensates in the following buffer (25 mM Tris-HCl pH 7.4, 75 mM KCl, 1.25% glycerol, 0.5 mM DTT, 5% PEG 8K) were dialyzed in a buffer of identical composition except it lacked the molecular crowder, PEG 8K. The dialysis was carried out using a 50 μl slide-a-lyzer dialysis cassette (20K MWCO membrane) at room temperature for overnight. This led to the loss of large condensates. Adding back PEG 8K to a final concentration of 5% (v/v) to the dialysis buffer led to the re-formation of large condensates. A control sample maintained at 5% PEG (v/v) all throughout this time did not show any such changes.

- **In vitro *RNA binding microscopy***

Labeled Vts1 condensates formed *in vitro* were incubated with RNAs labeled with fluorescein at their 5′ ends (GE Dharmacon) for 1 h at room temperature. The RNA sequences used were as follows: SRE+, harboring the cognate binding site was – $^{5'}$UAAUAAUC AGCUGGCCUGAUUAGUC3′; the permuted control SRE – had the following sequence - 5′UAAUAAUCAGGUCGCCUGAUUAGUC$^{3'}$ (see Key Resources Table for additional details). Following this incubation, these samples were imaged using fluorescence microscopy. The fluorescence intensity of the RNA colocalized with Vts1 condensates was measured using ImageJ.

- ***Negative stain EM of assemblies***

Purified protein samples were placed on formvar and carbon coated copper grids that had been glow discharged using standard procedures. The samples were stained using 1% (w/v) Uranyl acetate and imaged at 120kV using JEOL JEM-1400 TEM and images were collected using a Gatan Orius digital camera at the Stanford Electron Microscopy Core. The NM-Sup35 fibrils (Frederick et al., 2015) used as a morphological benchmark were a kind gift from Dr. Kendra Frederick, UT Southwestern Medical Center. Particle roundness of individual particles across fields of view was measured in imageJ.

- ***Proteinase K reactivity***

85 μl of labeled Vts1 condensates were incubated with 6 ul of proteinase K (Fisher) at room temperature (molar ratio of 1:6500 proteinase K: purified labeled Vts1). At each time point, a 12 μl aliquot was withdrawn from the reaction mixture and added to 2.4 μl of 6X Laemmli buffer. Following a 5 min heat denaturation, this sample was immediately placed on ice. A t0 sample was withdrawn before the addition of proteinase K. An identical procedure using an identical amount of unassembled Vts1 protein was followed for an unassembled Vts1 control. At the end of the time course, all samples were run on a 4%–12% SDS-PAGE gel, silver stained and imaged using a BioRad gel doc. Bands were quantified using Image Lab (Biorad) and relative proteolytic stability was measured as the ratio of the intensity of the full-length protein band at the end of the time course over the beginning of the time course across experimental replicates.

- ***Fluorescence recovery after photobleaching (FRAP) experiments***

FRAP experiments were performed on Vts1 condensates on a fully automated widefield fluorescence microscope system (Intelligent Imaging Innovations, 3i). Recovery of a bleached spot inside Vts1 condensates was measured and normalized FRAP intensity was analyzed using the following equation –

$$I_{frap-norm(t)} = \left[I_{ref-pre} \Big/ \left\{I_{ref(t)} - I_{base(t)}\right\}\right] \times \left[\left\{I_{frap(t)} - I_{base(t)}\right\} \Big/ I_{frap-pre}\right]$$

$I_{ref\text{-}pre}$ and $I_{frap\text{-}pre}$ were the mean intensities of the bleached spots and a reference unbleached spot prior to photobleaching. $I_{ref(t)}$, $I_{base(t)}$, and $I_{frap(t)}$ are intensities of a reference unbleached spot, background spot and bleached spot of equal radius at a given time (t). Images were collected before photobleaching (*for correction*) and up to 5 min after photobleaching for three independent condensates. These images were registered using rigid body transformation and intensity traces were corrected for photobleaching, normalized and this normalized intensity was plotted against time (Thévenaz et al., 1998). All analyses was done in ImageJ (Schneider et al., 2012).

Yeast native lysate extraction

Cells as specified were harvested from cultures (100 ml) in the mid-exponential phase by centrifuging at 5000 g for 2 min at 4°C. All subsequent steps were performed at that temperature or below as stated and the method followed was based upon lysate extraction for biochemical reconstitution of nucleic acid processing assays (Heller et al., 2011). Cells were washed twice with wash buffer (50 mM HEPES-NaOH (pH 7.6),2 mM EDTA, 0.8 M sorbitol, 300 mM Sodium glutamate, 3 mM DTT *added fresh* right before use) and resuspended in 1/2 packed cell volume of lysis buffer (100 mM HEPES-NaOH (pH 7.6), 0.8 M sorbitol, 950 mM Sodium glutamate, 10 mM Magnesium acetate, 5 mM DTT and 1 Complete protease inhibitor cocktail tablet per 5 mL added right before use). This resuspensate was then frozen dropwise in liquid nitrogen and the resultant beads were stored at −80°C until needed. Yeast cell beads were loaded into a steel vial pre-chilled at −80°C and processed using a cryo mill (Retsch) using the following program

sequence (1.5 min precooling at 5 Hz, 9 cycles of 2 min each at 15 Hz, 30 s of gap at 5Hz in between each cycle). The resulting powder was transferred using a prechilled spatula to a sterile conical tube and completely thawed on ice. Taking an aliquot from a dilution of this sample, we confirmed complete lysis of the yeast cells under the microscope. Next, we added lysis buffer to this mixture (1/3rd of the total volume) and transferred the sample to an eppendorf tube. This lysate was then centrifuged at 4°C, first at 10,000 g for 2 min to get rid of cell debris and then followed up with an additional spin at 500 g for 15 min. The resultant supernatant is dialyzed (using a 10 kDa MWCO membrane) to reduce the salt concentration and introduce glycerol for storage at −80°C overnight using dialysis buffer (50 mM HEPES-NaOH (pH 7.6),2 mM EDTA, 10% (v/v) glycerol, 300 mM Sodium glutamate, 5 mM Magnesium acetate, 3 mM DTT *added fresh* right before use). Total protein concentration is measured by A_{595} and using the Bradford assay reagent and aliquots of the lysates were stored at −80°C.

Affinity precipitation

Lysates prepared from native lysis of CCR4-GFP and POP2-GFP tagged strains were prepared as detailed above. Next we generated Vts1-SNAP^{Biotin} tagged protein and generated Vts1-SNAP^{Biotin} condensates using crowders as described above. As previously, Vts1 concentrations were measured by A_{595} and using the Bradford assay reagent against a standard curve. These lysates were incubated at 4°C for 2 h with nutation with identical amounts of Vts1-SNAP^{Biotin} condensates or Vts1-SNAP^{Biotin} samples where no crowder was added (see Figure S4B for *schematic*). Following this incubation, Dynabeads^{TM} M-280 Streptavidin were added to this mixture and incubated for 1 h at 4°C to allow interaction with Vts1-SNAP^{Biotin}. These streptavidin coated magnetic beads were then washed twice with PBS and any affinity precipitated protein was eluted of the beads by incubating with 0.1% SDS for 5 min at 95°C. These eluates were probed for the presence of GFP tagged proteins using anti-GFP antibody. A control experiment for non-specific affinity precipitation was conducted following identical steps but using SNAP-only^{Biotin} samples both in presence and absence of crowder.

In vivo RNA decay measurements

Yeast strains as indicated (naive, [*SMAUG*$^{+}$], *vts1Δ* and cured [*SMAUG*$^{+}$] strains) were transformed with a galactose inducible GFP-SRE reporter plasmid marked with *HIS* selection marker (a gift from C. Smibert, Univ. of Toronto) (Rendl et al., 2008). These strains were plated on a SD-His medium and three independent transformants for each strain were then patched onto a SD-His plate and grown overnight. These three independent biological replicates were then grown in SRaf-His medium upto saturation for 48 h. These cultures were diluted 1:100 in fresh SRaf-His medium (50 ml) and grown to a mid-exponential state (OD_{600} ~0.8). Samples were collected for RNA extraction as outlined by Smibert and colleagues (Rendl et al., 2008). In brief, the incubating temperature of the strains was reduced to 20°C (as the RNA species to be detected is too labile at the normal yeast growing temperature of 30°C) for 1 h. Cultures were spun down, washed once with sterile water and the medium was changed to inducing medium of SGal-His (containing 2% galactose). This medium turns on the expression of the GFP-SRE cassette. After 16 minutes in this medium, the induction was shut off by adding glucose to a final concentration of 4%. A T0 sample was taken before the addition of glucose and at several time points upto 1 h, a 1 mL aliquot of the cultures were collected, rapidly spun down and immediately frozen on dry ice. In parallel, this was also done for control yeast strains that were transformed with the permuted SRE reporter.

Individual gene expression measurements

RNA was extracted from all the samples collected above using the hot-phenol protocol (Collart and Oliviero, 2001). The cell pellets were resuspended in 200 μL TES solution (10 mM Tris-HCl pH 7.5, 10 mM EDTA, 0.5% SDS), 200 μL acid phenol pH 4.3 (Fisher) was added and the mix was vortexed vigorously for 10 s. The sample was incubated for 60 min at 65°C with periodic vortexing every 15 min and then placed on ice for 5 min. Samples were microcentrifuged for 10 min at 20,000 x *g* at 4°C. The aqueous (top) phase was transferred to a clean 1.5 mL microcentrifuge tube and 200 μL of chloroform was added. The tube was vortexed vigorously, spun and the aqueous phase was transferred to a new tube. Nucleic acid from this sample was then ethanol precipitated as follows - we then added 1/10th (v/v) of 3M sodium acetate pH 5.2 and 3x volumes of cold 100% ethanol, and RNA was precipitated overnight at -20°C. The RNA was microcentrifuged as before, the pellet washed with cold 70% ethanol, air-dried and resuspended in 45 μl of DEPC treated (RNase free) water. We removed residual DNA using Ambion Turbo DNA-free kit following manufacturer's instructions. We prepared cDNA using an oligo-dT(20) primer (Invitrogen) and SuperScript® Reverse Transcriptase II (Invitrogen), and performed quantitative real-time PCR with SYBR green detection (QIAGEN) probing for GFP mRNA signal. Primers against housekeeping gene *TAF10* were used as controls for relative quantification (Teste et al., 2009).

Yeast microscopy

Single colonies of yeast strains with either the GFP-SRE reporter or the permuted control were incubated in SRaf-His medium then grown upto saturation for 48 h. These cultures were diluted 1:100 to a total volume of 200 μl in 96 well plates in fresh medium whose sugar composition was as follows – 0.1% galactose and 1.9% raffinose. Cells were grown in this medium overnight and steady state GFP protein levels were measured by imaging these cells using 100x objective on the fluorescence microscope. All DIC and fluorescence images (GFP channel) across samples were exposed identically. Quantification of GFP intensity was carried out for individual cells as indicated for each strain using CellProfiler (Kamentsky et al., 2011). All scale bars used are 5 μm unless otherwise mentioned.

Construction of endogenous [SMAUG$^+$] reporter and growth phenotyping assays

The *ynr034w-a*::URA3 strain for studies of [*SMAUG*$^+$] was constructed as follows. A URA3-SpHIS5 cassette was amplified from a modified pUG27 plasmid (used earlier for [*MOT3*$^+$] prion, (Alberti et al., 2009), a kind gift of Randal Halfmann, Stowers Institute, Missouri. Forward and reverse primers for amplification of the cassette contained 93bp and 81bp of homology immediately up- and down-stream from the *YNR034W-A* open reading frame (Upstream: 034W-A_KO_5′ END; Downstream: 034W-A_KO_3′ END, see Key Resources Table). This PCR product was gel-purified and transformed by electroporation *(described above)* into naive, [*SMAUG*$^+$] and *vts1Δ* yeast strains. Transformants were selected on SD-His plates and correct integration was confirmed by amplifying across 5′ and 3′ integration junctions with the following primer pairs respectively - YNR034W-A::UraHisCass_confA & UraHisCass_confB and UraHisCass_confC & YNR034W-A::UraHisCass_confD (see Key Resources Table).

The reporter strains constructed above were streaked out into single colonies on a YPD plate as detailed above. Four individual colonies were inoculated into 150 μl of YPD liquid medium and grown in a 96 well plate overnight at 30°C minimizing evaporation from the wells by filling empty wells around the wells of interest with sterile water. Following this overnight growth, the cells were diluted to an OD_{600} of 0.15 and grown till mid-exponential OD_{600} of 0.6. The number of cells in these mid-exponential cultures were then counted using a hemocytometer and 150 μl of SD-Ura liquid medium was inoculated with ~300 cells. The OD_{600} of these cultures were measured over a 96 h time course with continual shaking at 30°C and lag times were extracted from these growth curves.

Protein transformation

Mid-exponential cultures of *ynr034w-a*::URA3 reporter strains constructed in naive and *vts1Δ* backgrounds were washed with sterile water and 1 M sorbitol. The cell pellets were finally resuspended in SCE buffer (1M sorbitol, 10 mM EDTA, 10 mM DTT, 100 mM Na-Citrate pH 5.8). This resuspensate was then adjusted to 0.55 – 1.83 U/ml of Zymolyase®-100T (amount depended on genetic background) and incubated at 37°C for 10 −15 min to make spheroplasts. These spheroplasts were pelleted by a gentle spin, washed with 1M sorbitol, and resuspended in STC buffer (1 M sorbitol, 10 mM $CaCl_2$, 10 mM Tris pH 7.5) by a gentle tap on the culture tube walls. All subsequent steps involving liquid transfer of these spheroplasts were done with 1 mL pipette tips that had been blunted by cutting with a sterile razor blade. These spheroplasts were incubated with salmon sperm DNA, carrier plasmid with a *LEU2* marker (pAG415-GPD-ccdB, (Alberti et al., 2007), and Vts1-SNAP protein or BSA (at 1 μM) at room temperature for 30 minutes. Fusion was induced in these spheroplasts by adding 9 volumes of PEG buffer (20% (w/v) PEG 8000, 10 m*M* $CaCl_2$, 10 m*M* Tris, pH 7.5) and incubating at room temperature for 30-60 minutes. These reaction conditions concomitantly generated Vts1 condensates from full-length protein. These spheroplasts were collected and finally resuspended in 250 μl of SOS buffer (1M sorbitol, 7 m*M* $CaCl_2$, 0.25% yeast extract, 0.5% bactopeptone) by pipetting with cut pipette tips. This mixture was incubated at 30°C for 3 h after which these cells were plated on a SD-Leu solid media that had been supplemented with 1.2 M sorbitol. Following plating, these cells were overlaid with a soft agar (0.8% agar) of an otherwise identical composition and the plates were incubated at 30°C for 3 – 5 days. Individual LEU$^+$ transformants (31 to 43; WT-naive cells: Vts1 condensates – 43 transformants, BSA - 42 transformants; *vts1Δ* cells: Vts1 condensates – 31 transformants, BSA – 31 transformants) were picked and phenotyped in SD-Leu-Ura liquid medium as described in endogenous [*SMAUG*$^+$] reporter assays above. Since protein transformation requires incubating the protein with PEG 8000, these experimental conditions lead to the co-formation of Vts1 condensates. So, in parallel, we performed analogous experiments with BSA as a control (which does not form condensates under these conditions, Figure S2H). A parallel set of experiments was done using GFP-SRE reporter and measuring the GFP fluorescence in transformants arising from transformation with Vts1 condensates or BSA alone (Figure S4H).

Library preparation and RNA sequencing and analyses

RNA sequencing was performed on two biological replicates of naive, [*SMAUG*$^+$] and *vts1Δ* cells each. 50 mL cultures of these strains were grown to mid-exponential phase (OD_{600} ~0.6), pelleted, and snap frozen in liquid nitrogen. From all samples, RNA extraction and library preparation was performed using standard kits (stranded, Ribo-Zero rRNA removal). All samples were sequenced to ~30,000,000 read depth (1 × 50 bp) on one lane of an Illumina HiSeq 4000^{TM}. Quality control of reads were performed using FastQC (Babraham Institute). Reads were deduplicated, pseudoaligned against the *Saccharomyces cerevisiae* strain S288C reference genome assembly R64 and transcript-level quantification was performed using Kallisto (Bray et al., 2016). Differential expression analyses were performed using DESeq2 package in R (Love et al., 2014). Principal component analyses of most differentially regulated genes and significantly altered transcripts were called using default settings in the DESeq2 package which employ Benjamini-Hochberg approach that approximated the false discovery rate (FDR). RNA-seq data are deposited to Gene Expression Omnibus (GSE138557).

Strain Design and Competition asays

A *TDH3* promoter driven fluorescent protein (either mKate2 or mNeonGreen; kate and neon hereafter) cassette was amplified from the following plasmids - pSK275_pTDH3_mKate2 (see Key Resources Table) and pSK275_pTDH3_Neon (see Key Resources Table) using pSK-HO-F and pSK-HO-R primers. These plasmids were a kind gift from Brandon Wong of the Khalil lab, Boston University and allowed us to clone a fluorescent protein marker into WT-naive and WT-[*SMAUG*$^+$] strains under the control of a *TDH3* constitutive promoter and a hygromycin-selectable marker into the HO locus. Individual hygromycin transformants were selected on

YPD + 200 μg/L hygromycin B and correct integration was confirmed using primers flanking the 5′ and 3′ integration junctions using following primers HO pSK275 Homology Region Reverse 1 & HO pSK275 Homology Region Forward 1 and SSB1 pSK275 Homology Region Reverse 2 & SSB1 pSK275 Homology Region Forward 2 (see Key Resources Table). Strains were further confirmed to be expressing the fluorescent protein by imaging with a fluorescence microscope (Leica DMI6000). Growth curves of each PCR-confirmed, fluorescent transformant was generated to ensure that the exogenous fluorescent protein expression did not result in an obvious growth defect. We generated Neon-tagged WT-naive and WT-[*SMAUG*$^+$] as well as Kate-tagged WT-naive and WT-[*SMAUG*$^+$] strains. These Neon and Kate expressing strains were pre-grown for 48h in synthetically defined medium containing 2% galactose. Strains were diluted to an OD_{600} of 0.1. Competitions were carried out by mixing a Neon strain and a Kate strain in a 1 to 1 ratio, and inoculating 1 μl of this mixture into SD-CSM media containing 2% glucose (150 μl). These mixed cultures were incubated at 30°C for 48 hours in a 96-well plate. We used water filled capping plates to minimize loss of liquids by evaporation. After 48 h, we took a 100 μl aliquot of this mixed culture and fixed it using 4% paraformaldahyde for 15 minutes and stored in 1.2M sorbitol 0.1M potassium phosphate at 4°C until flow cytometry analysis. The remaining co-culture was diluted to an OD_{600} of 0.1 using sterile water; 1 μl of this dilution was used to inoculate a fresh batch of SD-CSM media and the competition in the orthogonally tagged strains was restarted. Flow cytometry measurement was done on the Scanford instruments in the Stanford Shared FACS Facility exciting at 488nm for Neon and 561nm for Kate. Ten thousand yeast cells (gated using standard forward and side scatter parameters) per sample was collected and the ratio of neon to kate signal was analyzed using FlowJo v10.2. To correct for any tag-specific growth effects, control competitions where the same strain was marked with different fluorescent protein tags (i.e., WT-naive expressing Kate competed with WT-naive expressing Neon) were also performed. Any difference in growth observed in these competitions was treated as a tag-specific growth effect and normalized for when looking for strain specific growth difference. Additionally, we swapped the fluorescent protein markers for the strains and conducted a competition experiment in parallel. The data of the ratio of neon/kate signal was then fit to a linear regression model, the slope of which is a measure of the selection coefficient for a particular strain.

Purification and labeling of human Smaug homolog (hSmaug1)

cDNA encoding for SAMD4A or hSmaug1 (human homolog of Vts1) was synthesized (Genscript) and Gibson assembled into a T7 driven expression system (see Key Resources Table). Protein expression was induced in a similar way described above for yeast Vts1 proteins and the target fraction was purified using a combination of chromatographic steps including Ni-affinity, SP-Sepharose ion exchange, FLAG affinity and finally a Superdex200 Increase (GE) gel filtration column. Labeling and subsequent cleanup of the excess dye was performed as detailed above for yeast Vts1 proteins.

Seeding assay in yeast

The test for seeding of hSmaug1 was performed in a similar way as described before (Chakrabortee et al., 2016). In brief, the hSmaug1 cDNA was assembled to construct a gateway entry clone (see Key Resources Table). This construct was then cloned into an expression vector (marked with *URA3* auxotrophy; pAG426 backbone, see Key Resources Table; Alberti et al., 2007) under the control of a galactose inducible promoter that tagged hSmaug with a C-terminal GFP. This construct was transformed into yeast using standard protocols described above. Transformants were grown to saturation in a low expression medium that did not induce the formation of foci (per liter in water: 6.7 g yeast nitrogen base with ammonium sulfate, 0.77 g CSM –Ura powder (Sunrise Science Cat# 1004-100), 20 μg galactose and 19.98 g raffinose) and cells were then imaged 'pre-induction' (exposure time ~500 ms). Following this, cells were gently spun down, low expression media was removed, and cells were re-suspended in high-expression media (per liter in water: 6.7 g yeast nitrogen base with ammonium sulfate, 0.77 g CSM –Ura powder (Sunrise Science Cat# 1004-100), 5 g galactose and 15 g raffinose). After overnight (~16 h) induction, the cells were re-imaged for 'induction' phase (exposure time ~50 ms). These induced cells were washed with water and then diluted 400-fold back into low-expression media and allowed to grow for 48 hr to saturation before being imaged one last time for the 'withdrawal' phase (exposure time ~500 ms). As a control, an identical workflow was performed in parallel for a GFP-only construct.

QUANTIFICATION AND STATISTICAL ANALYSIS

Quantification and accompanying statistical tests for all experiments are described in the Results section, STAR Methods, and figure legends. The Welch's t test test was used to compare measurements between two sets of samples unless otherwise mentioned. Fisher's exact tests and hypergeometric tests were used to compare overlap between sets of transcripts and proteins. *p-value*s < 0.05 were interpreted as reflecting significant differences.

DATA AND CODE AVAILABILITY

All gene expression data collected are deposited in Gene Expression Omnibus (GEO) under accession number GSE138557. Representative microscopy images and raw gel images have been submitted to Mendeley (10.17632/gzc6z9dkhy.1).

Molecular Cell, Volume *77*

Supplemental Information

A Non-amyloid Prion Particle that Activates a Heritable Gene Expression Program

Anupam K. Chakravarty, Tina Smejkal, Alan K. Itakura, David M. Garcia, and Daniel F. Jarosz

SUPPLEMENTAL INFORMATION
Supplemental Figures

Figure S1, related to Figure 1

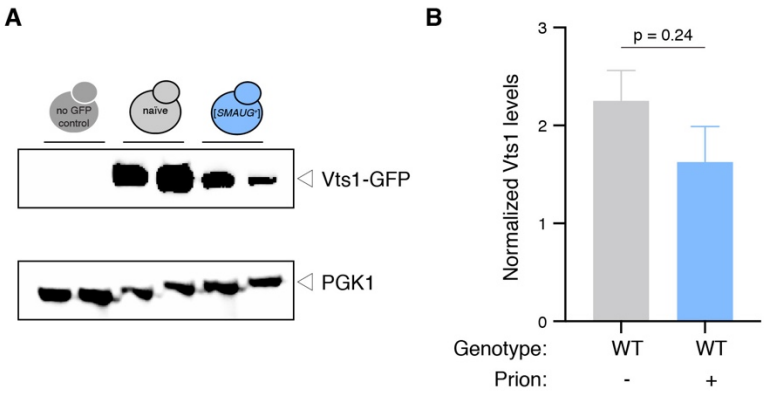

Figure S1: Vts1 levels are similar in naïve and [*SMAUG*$^{+}$] cells. (A) Representative Western blot depicting levels of Vts1 protein in naïve and [*SMAUG*$^{+}$] cells relative to a loading control Phosphoglycerate kinase 1 (Pgk1). Separate lanes correspond to different biological replicates of naïve, [*SMAUG*$^{+}$] and no GFP-control cells. (B) Normalized levels of Vts1-GFP polypeptide relative to Pgk1 loading control across four replicates. p – value from Welch's t-test for the indicated comparison have been explicitly stated.

Figure S2, related to Figure 2

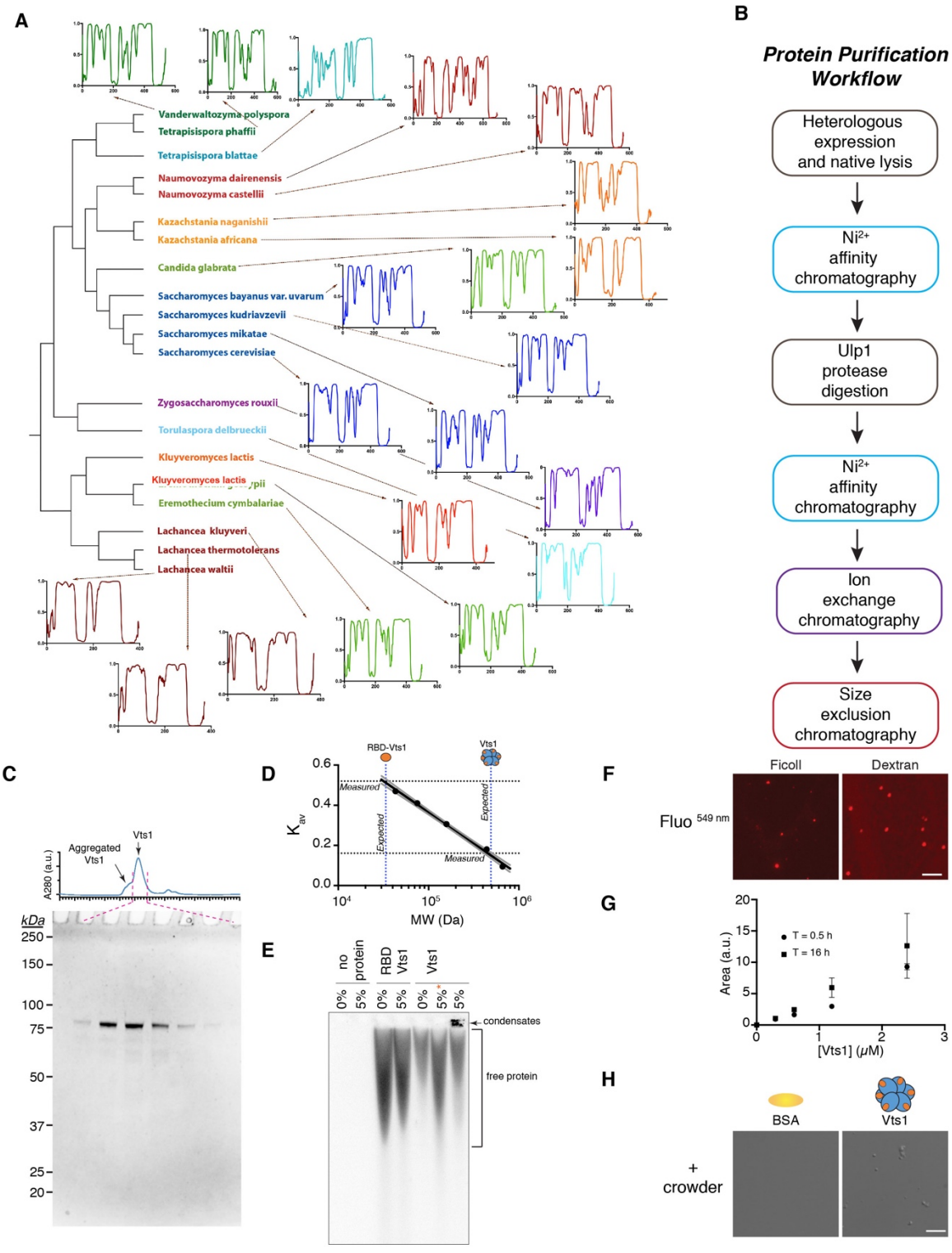

Figure S2: Overview of intrinsic disorder in Vts1 homologs, and purification and functional testing of *S. cerevisiae* Vts1. (A) Individual disorder probability plots of fungal Vts1 homologs.

(B) Protein purification workflow used for Vts1, IDR-Vts1 and RBD-Vts1. (C) Size exclusion chromatography traces and Coomassie-stained SDS-PAGE gel of the corresponding fractions. The size markers used for the gel are also depicted. (D) Standard curve of partition coefficient with molecular weight, as determined on the Superdex200 Increase size exclusion column using the following size markers: thyroglobulin (660 kDa), ferritin (440 kDa), aldolase (158 kDa), conalbumin (75 kDa), ovalbumin (43 kDa). The gray lines indicate the 95% confidence interval from three individual runs of the size markers, and the dotted lines demarcate the measured partition coefficients and expected molecular weights. (E) Native agarose gel electrophoresis (NAGE) of Vts1 and RBD-Vts1 under the indicated conditions. The lane marked with an orange * represents a control in which the crowder was added immediately prior to electrophoresis. (F) Phase separation of labeled Vts1 using different molecular crowders as indicated above. (G) Mean area ± SEM across three technical replicates of the Vts1 condensates across concentrations and times as indicated. (H) DIC images of BSA (control protein) and Vts1 (non-SNAP tagged) in presence of macromolecular crowder (5% PEG-8000).

Figure S3, related to Figure 3

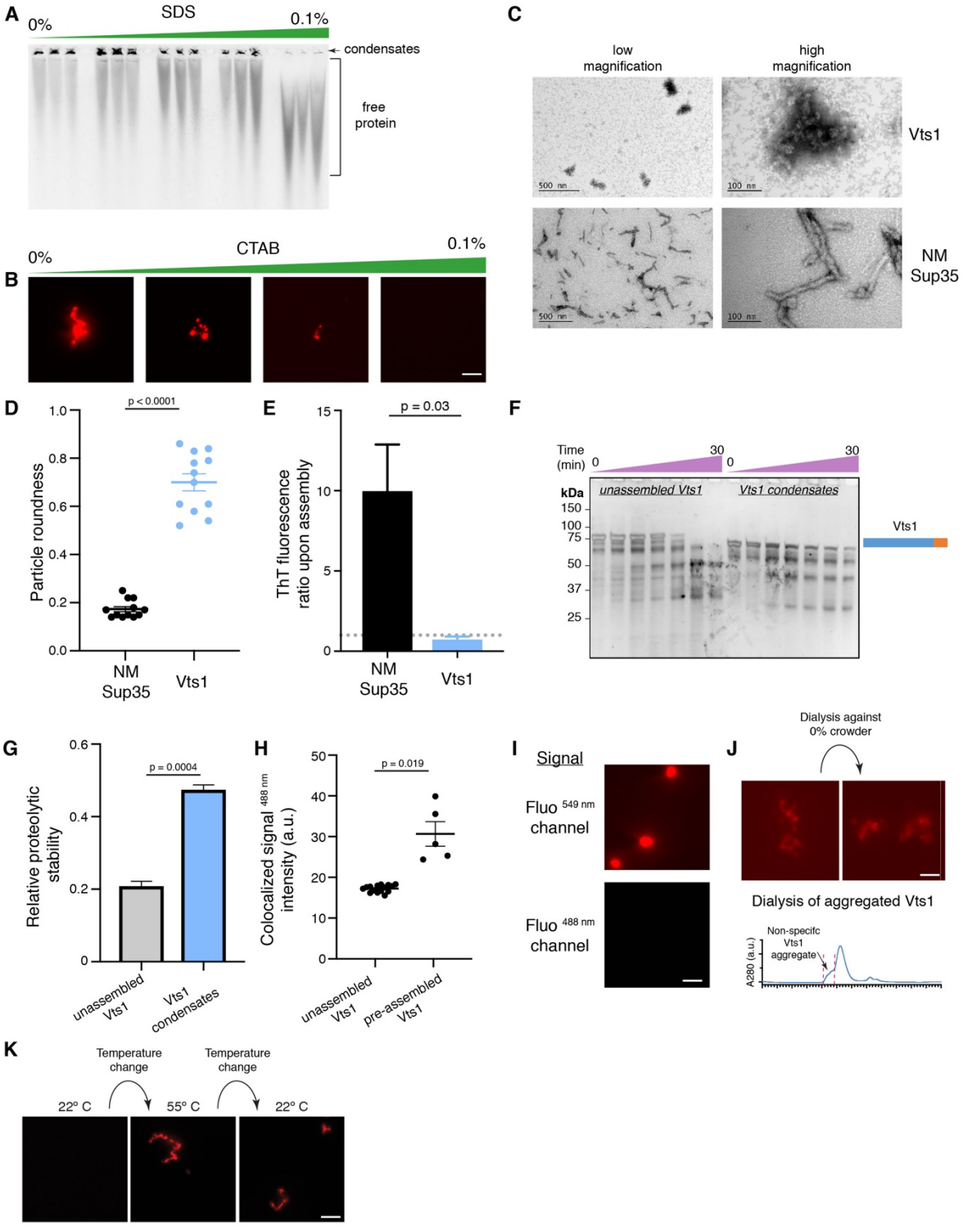

Figure S3: Detailed biochemical properties of Vts1 condensates. (A) SDS sensitivity of Vts1 condensates as measured in NAGE assays. (B) Cetyl trimethyl ammonium bromide (CTAB) sensitivity of Vts1 condensates. Representative images are in the concentration gradientof CTAB as depicted above. (C) Representative negative stain transmission electron microscopy images of Vts1 condensates and morphological benchmark Sup35-NM fibers at two different magnifications. Vts1 condensates are in the following buffer - 25 mM Tris-HCl pH 7.4, 75 mM KCl, 1.25% glycerol, 0.5 mM DTT, 5% PEG 8K while the morphological benchmark is in CRBB buffer (5 mM Potassium phosphate pH 7.4, 150 mM NaCl). (D) Quantification of particle roundness across several particles as observed in negative stain transmission electron microscopy of Vts1 condensates (blue) and Sup35-NM sample (black). Mean±SEM for all particles is depicted and the p-value for the difference in means was determined using Welch's t-test. (E) Increase in Thioflavin-T fluorescence upon assembly of Vts1 condensates (blue) or NM-Sup35 fibrils (black). Gray dotted line represents the ratio of fluorescence change in buffer-only control. Samples are in buffer as mentioned above. p-value was determined for the difference in the means using Welch's t-test. (F) Proteinase K susceptibility assays of Vts1 condensates and unassembled Vts1 over the indicated time periods. The SDS-PAGE gel was silver stained, and the intensity of the top band was tracked. Note that addition of crowder altered electrophoretic mobility of Vts1 slightly, even before the action of proteinase K (0 min time point). (G) Relative proteolytic stability of Vts1 condensates (blue) with respect to unassembled Vts1 (gray) measured as the ratio of the top-most band at the end of the timecourse relative to its start. Mean±SEM for three replicates is depicted and the p-value for the difference in means was determined using Welch's t-test. (H) Colocalized signal $^{488\ nm}$ in co-assembly experiments with unassembled Vts1 versus pre-assembled Vts1 as stated. Representative micrographs have been shown in Figure 3C. Mean±SEM of intensity for all colocalization events in pre-assembled Vts1 sample is depicted. For unassembled sample, mean±SEM intensity of a mask of similar area has been depicted. p-value for the difference in means was determined using Welch's t-test. (I) Controls demonstrating

that bleeding of the $SNAP^{549}$ signal into the GFP channel was negligible. Images were collected under the same imaging and contrast conditions used for co-seeding experiments (*in Figure 2C*). (J) Irreversibility of non-specific Vts1 aggregates formed by addition of crowder to pre-aggregated Vts1. (K) Phase separation of Vts1 by heat is not reversible. Temperatures are indicated above each micrograph. All microscopy scale bars used are 5 μm.

Figure S4, related to Figure 3 & 4

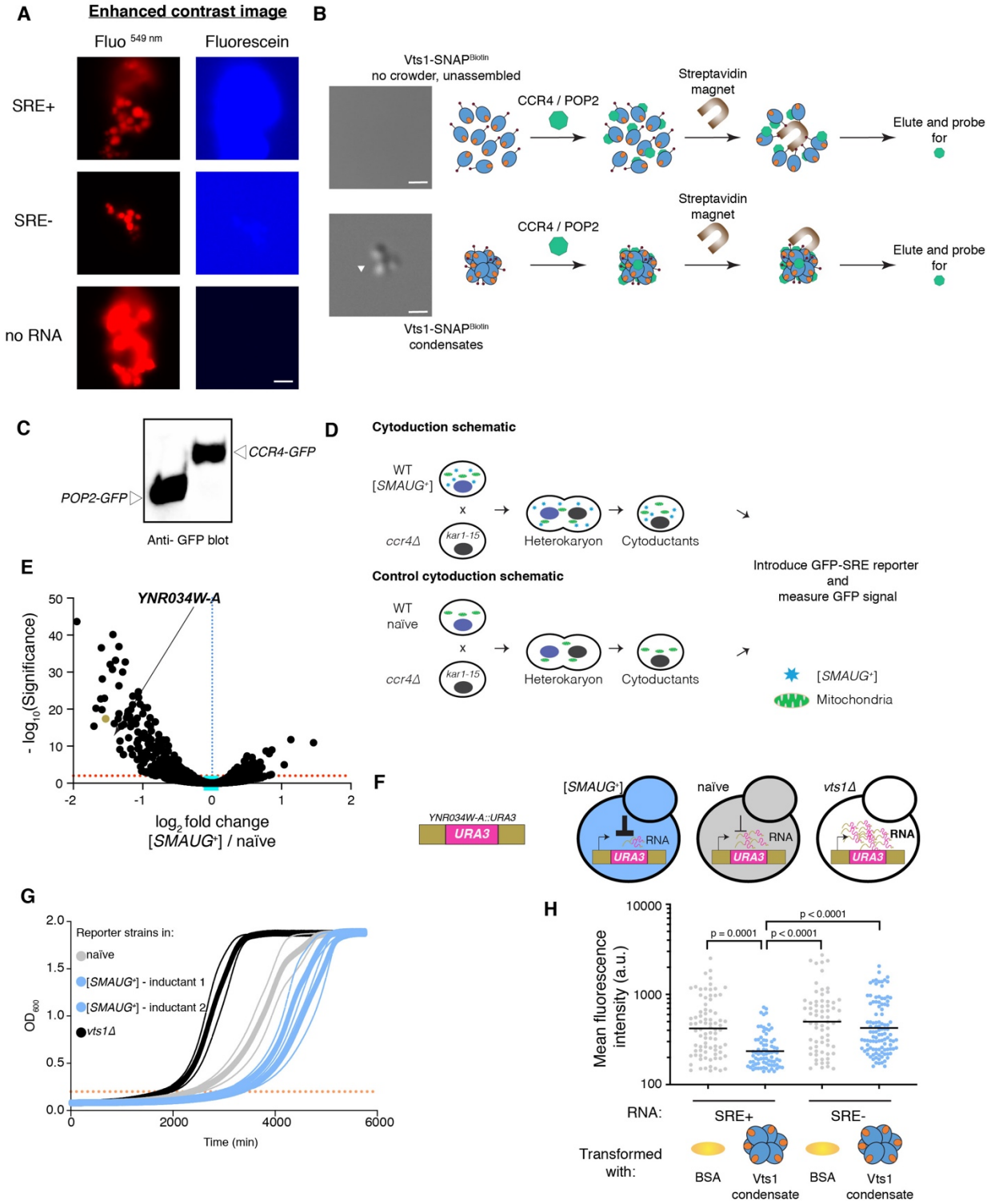

Figure S4: Functional interactions of [*SMAUG*$^{+}$] and construction of the endogenous [*SMAUG*$^{+}$] reporter. (A) Vts1 condensates formed *in vitro* bind RNA. Representative images of labeled Vts1 condensates (SNAP^{549} channel in red), SRE-RNA (fluorescein channel in blue), and their overlay (in magenta) are shown. Two different kinds of SRE-RNAs were used: SRE+, cognate binding sequence (top row); SRE-, permuted sequence that is not recognized by Vts1 (middle row) and no RNA sample (bottom row). The contrast has been significantly enhanced for all fluorescein panels over Figure 3F to reveal background fluorescein signal in SRE- sample. Scale bar is 5 μm. (B) Representative DIC micrographs of Vts1-SNAP^{Biotin} sample in the absence (above) and presence (below) of crowder. Condensates are formed in the presence of crowder (below). Schematic of affinity precipitation experiment to investigate the capacity of Vts1 condensates to recruit effectors. Scale bar in the top panel is 5 μm and bottom panel is 1 μm. (C) Representative Western blot of native lysates obtained from GFP tagged CCR4 and POP2 strains. (D) Schematic of cytoduction experiment conducted in Figure 3I. (E) Volcano plot of -$\log_{10}$(adjusted p-values) vs $\log_2$(fold change) of mRNA abundances in [*SMAUG*$^{+}$] relative to naïve cells across the entire transcriptome. The blue dotted line denotes no change in transcript levels. Points to the left of this line indicate lower abundance in [*SMAUG*$^{+}$] relative to naïve cells; points to the right indicate higher abundance. The red dotted line indicates the significance cutoff (FDR=1%; Benjamini-Hochberg) used for analyses. The teal square indicates the ratio of RNA abundance in [*SMAUG*$^{+}$] vs. naïve cells for a housekeeping mRNA, *ACT1*. The yellowish-green dot indicates the transcript *YNR034W-A*, which was engineered to construct the reporter. (F) Schematic of the endogenous reporter construct and its activity in the indicated strains. (G) Growth curve of these reporter strains in medium lacking uracil, starting from nearly identical ODs. x-intercepts from where the orange dotted line intersects the growth curves represents the lag time measurement for that strain. (H) Mean GFP fluorescence intensity of cells harboring GFP-SRE+ or GFP-SRE- reporter as stated and transformed with BSA or Vts1 condensates as depicted. The p-values are calculated using Tukey's multiple test.

Figure S5, related to Figure 5

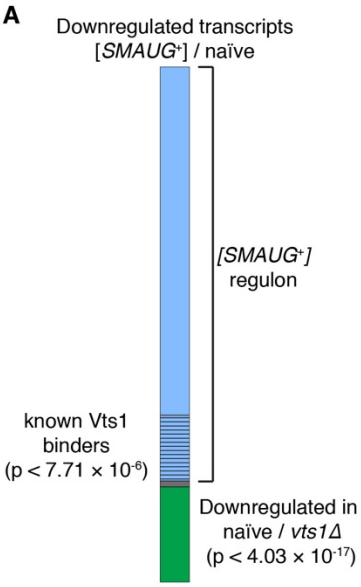

C

Gene Ontology terms	FDR
Carbohydrate transport	5.15×10^{-6}
Energy reserve metabolic processes	5.65×10^{-6}
Glycogen metabolic process	3.22×10^{-5}
Cellular carbohydrate metabolic process	3.22×10^{-5}
Carbohydrate transmembrane transport	3.71×10^{-5}
Single-organism carbohydrate metabolic process	5.98×10^{-5}
Glucose transport	2.89×10^{-4}
Cellular polysaccharide metabolic process	3.52×10^{-4}
Regulation of generation of precursor metabolites and energy	3.59×10^{-3}
Generation of precursor metabolites and energy	6.70×10^{-3}
Response to pH	6.70×10^{-3}
Oxidation-reduction process	6.70×10^{-3}
Cellular response to salt stress	6.70×10^{-3}
Fructose transport	8.63×10^{-3}
Glycogen biosynthetic process	9.18×10^{-3}
Pentose transport	9.18×10^{-3}
Energy derivation by oxidation of organic compounds	9.18×10^{-3}
Regulation of glycogen metabolic process	9.18×10^{-3}

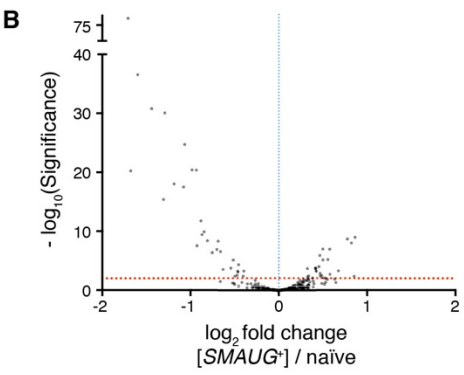

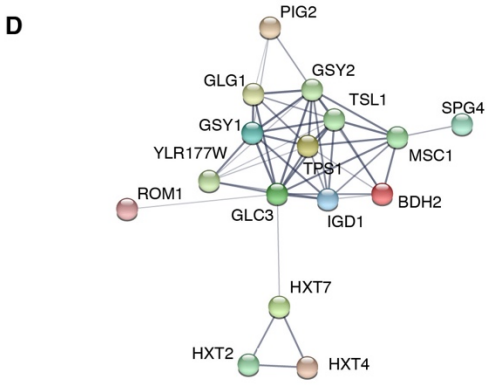

Figure S5: Additional analyses of the [*SMAUG*$^+$] regulatory network. (A) Nature of the transcripts downregulated in [*SMAUG*$^+$] over naïve cells classified according to their known interactions with native Vts1. (B) Volcano plot of -$\log_{10}$(adjusted p-values) vs. $\log_2$(fold change) of mRNA abundances in [*SMAUG*$^+$] relative to naïve cells, across the entire transcriptome for previously known Vts1 binders. The blue dotted line denotes no change in transcript levels. Points to the left of this line indicate lower abundance in [*SMAUG*$^+$] relative to naïve cells; points to the right indicate higher abundance. The red dotted line indicates the significance cutoff (FDR=1%;

Benjamini-Hochberg) used for analyses. (C) All significant Gene Ontology terms from the network and their corresponding false discovery rates (FDRs), corrected for multiple hypothesis testing by the Benjamini–Hochberg method. (D) Network summarizing physical and genetic interactions of transcripts that bind native Vts1 and are uniquely downregulated in [*SMAUG*$^{+}$] cells. Gene names for each node in the clusters are indicated.

Figure S6, related to Figure 6

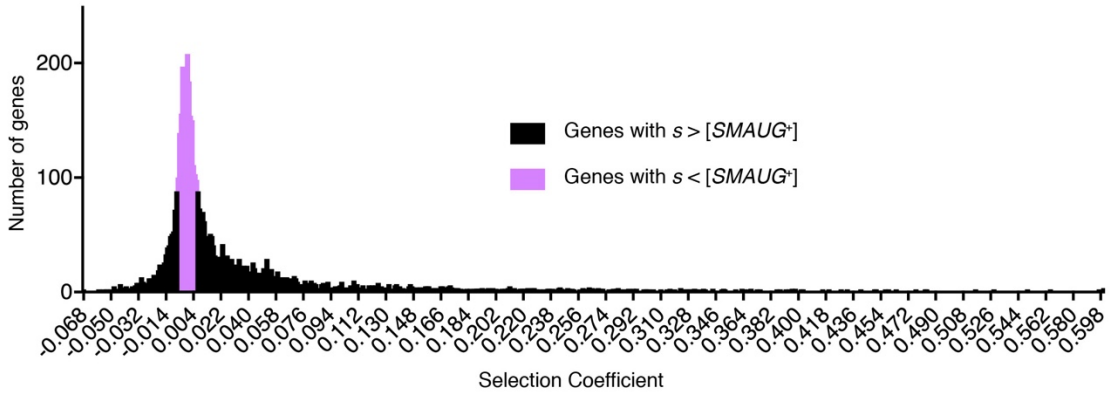

Figure S6: Distribution of selection coefficients of all genes in *S. cerevisiae.* Histogram of selection coefficients of all genes as measured in competition experiments (Breslow et al., 2008), used to benchmark the impact of [*SMAUG*$^{+}$]. The fraction in purple represents the more than one-third of all budding yeast genes for which the absolute value of the selection coefficient is lower than that of [*SMAUG*$^{+}$].

Figure S7, related to Figure 7

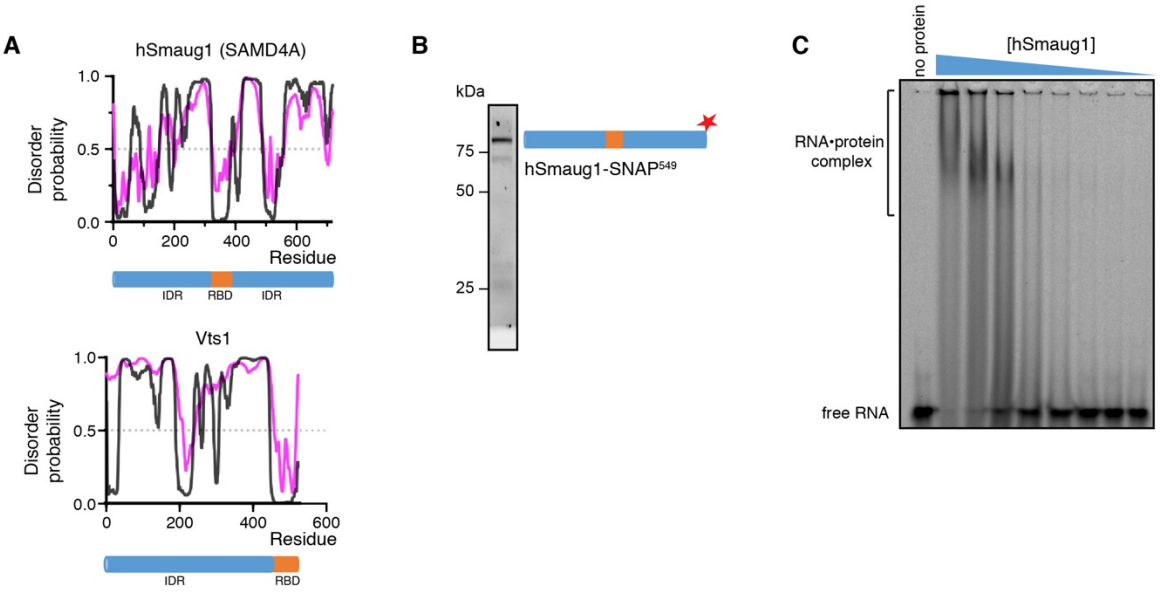

Figure S7: Purification of hSmaug1 and its functional validation. (A) Intrinsic disorder profile of hSmaug and Vts1 (from *S. cerevisiae*) computed using disopred (black) and VSL2 (purple) algorithms show presence of large disordered regions in these proteins. (B) SDS-PAGE gel of $SNAP^{549}$-conjugated hSmaug1. The markers used in the gel are indicated at left. (C) EMSA of hSmaug1 with a fluorescein-labeled SRE-containing RNA, imaged in the fluorescein channel. The leftmost lane is a control containing no protein; the remaining lanes contain a gradient of hSmaug1 (high→low concentration).